Loss of Synaptojanin 1 in dopamine neurons triggers synaptic degeneration and striatal TH interneuron compensation

Youneng Lin[1], Zhaoyan Li[1], Bandhan Mukherjee[1], Man Liu[1], Xiaoxing Cao[1], Zhen Wang[1], Hua Huang[,3], Zheng Ding[3] and Mian Cao[1,2]

1. Programme in Neuroscience and Behavioural Disorders, Duke-NUS Medical School, Singapore

2. Department of Physiology, National University of Singapore, Singapore

3. Electrophysiology Core Facility, Yong Loo Lin School of Medicine, National University of Singapore, Singapore 117544, Singapore

Authorship notes: Youneng Lin, Zhaoyan Li, Bandhan Mukherjee contributed equally.

Mian Cao is the corresponding author.

Bandhan Mukherjee present address: Department of Neuroscience, Johns Hopkins University School of Medicine, Baltimore, MD 21205, USA

The authors have declared that no conflict of interest exists.

Abstract

Synaptic dysfunction is an early feature of Parkinson's disease (PD). Synaptojanin 1 (SJ1), a phosphoinositide phosphatase linked to early-onset parkinsonism, is essential for clathrin-mediated endocytosis and synaptic vesicle recycling. While constitutive SJ1 mutant mice recapitulate patient-like phenotypes, their broad systemic effects obscure the cell type–specific functions of SJ1. Here, we report the first dopamine neuron–specific SJ1 conditional knockout (SJ1-DA cKO) mice. Complete and selective loss of SJ1 in dopamine neurons led to severe, widespread dystrophy of striatal dopamine terminals and impaired dopamine metabolism and release, demonstrating a cell-autonomous requirement for SJ1 in synaptic transmission across dopaminergic subtypes. Under chronic dopamine deficiency, SJ1-DA cKO mice showed reduced basal locomotion and exaggerated amphetamine-induced hyperlocomotion, but no obvious motor coordination deficits. Notably, we observed robust emergence of striatal induced tyrosine hydroxylase–positive interneurons (iTHINs) with unique dopamine-like properties and reduced GABAergic inhibition, indicating strong local adaptive plasticity that may partially compensate for dopamine deficiency. This adaptive response was absent in other PD lesion models and markedly limited when SJ1 was acutely deleted in adult dopamine neurons. Together, our findings establish SJ1's essential role in dopamine synapse maintenance and identify iTHIN induction as a potential compensatory mechanism with implications for PD interventions.

Introduction

Parkinson's disease (PD) is the second most common neurodegenerative disorder, primarily affecting movement. The pathological hallmarks of PD include the selective loss of dopamine (DA) neurons in the substantia nigra pars compacta (SNc) and DA deficiency in the striatum.

Although over 90% of PD cases are sporadic, recent genetic studies have identified more than 20 risk genes and 90 genomic risk loci associated with both familial and sporadic PD(1). Several of these genes regulate endocytic trafficking at presynaptic terminals, suggesting that impaired synaptic vesicle (SV) recycling is an early pathological feature of PD(2). A major SV recycling pathway involves clathrin-mediated endocytosis (CME), in which Synaptojanin 1 (SJ1), a lipid phosphatase, plays a crucial role(3). SJ1 facilitates clathrin uncoating by dephosphorylating PI(4,5)P_2 on the plasma membrane and releasing clathrin adaptors. In its absence, clathrin-coated vesicles (CCVs) accumulate at synapses, as demonstrated in multiple model organisms(4-7).

A homozygous missense mutation (R258Q) in SJ1 has been previously identified in early-onset Parkinsonism (EOP), establishing SJ1 as the PARK20 gene(8, 9). This mutation inactivates the Sac phosphatase domain, resulting in partial loss-of-function (LOF). Since then, additional SJ1 mutations have been linked to Parkinsonism and epilepsy, most of which are homozygous missense or nonsense mutations(2, 10). A strong genotype-phenotype correlation exists, where nonsense mutations causing premature truncation in the homozygous state led to severe neurodegeneration, seizures, and early mortality(11, 12). In contrast, homozygous or compound heterozygous missense mutations are associated with milder phenotypes, including Parkinsonism and seizure susceptibility(10, 13).

More recently, rare heterozygous SJ1 variants have been implicated in EOP, and Sac domain variants have been linked to sporadic PD(14). Additionally, a novel expression quantitative trait locus (eQTL) connection between rs10847864 and SJ1 was identified, highlighting convergence between familial and Genome-Wide Association Study (GWAS) studies(15). Furthermore, SJ1 expression is reduced in blood and postmortem PD brain tissues, suggesting it may serve as a biomarker for sporadic PD(16).

Multiple mouse models have been developed to study SJ1 LOF. Complete SJ1 loss in constitutive homozygous knockout (KO) mice results in early mortality and severe epilepsy,

mirroring human patients with homozygous nonsense mutations(11, 17). Aged SJ1-haploinsufficient (+/-) mice show PD-like features, including alpha-synuclein accumulation, autophagy defects, and DA terminal degeneration(18). They also exhibit impaired astrocytic glucose sensing and lysosomal dysfunction in midbrain neurons(19, 20).

Our previously generated SJ1 knock-in (KI) mice carrying the R258Q mutation (SJ1-KI^{RQ}) exhibit neurological symptoms reminiscent of EOP, including early-onset epilepsy and motor coordination deficits(21). These mice display generalized synaptic endocytic defects and selective synaptic degeneration in a subset of DA neurons in nigrostriatal pathway, a hallmark of PD pathology(21). Additionally, we demonstrated a synergistic interaction between SJ1 and auxilin (PARK19), another PD-linked clathrin uncoating protein(22). Auxilin-KO mice exhibit dystrophic nigrostriatal DA terminals similar to SJ1-KI^{RQ} mice. In double mutant (Aux-KO/SJ1-KI^{RQ}) mice, lifespan is dramatically reduced, and synaptic endocytic defects and striatal dystrophic changes are exacerbated, further supporting the vulnerability of nigrostriatal neurons to synaptic endocytic impairments(22).

Synergistic effects of SJ1 with other PD-linked proteins have also been demonstrated in double mutant mouse models. INPP5F/Sac2, a PI4P phosphatase involved in endosomal trafficking, has been identified as a PD risk gene through GWAS(23). Sac2-KO/ SJ1-KI^{RQ} mice show shortened lifespan, more severe endocytic defects, and earlier DA terminal dystrophy(24). In addition, combining SJ1 heterozygosity with LRRK2 G2019S worsens DA release deficits and motor impairments in aged mice(25).

While these mouse models have provided valuable insights into SJ1 function in PD, they are all constitutive whole-body mutants, leading to complex behavioral phenotypes and even early death due to global SJ1 loss in the brain. To better delineate SJ1's role in DA neurons in PD, we generated novel DA neuron-specific SJ1 conditional KO models (both genetic and acute deletions) in this study. Complete SJ1 loss in DA neurons of genetic cKO mice results in severe DA terminal dystrophy and DA deficiency throughout the striatum. These mutant mice exhibited reduced spontaneous locomotor activity but showed a marked increase in amphetamine-induced locomotion, likely due to enhanced sensitivity of downstream DA receptors. However, no obvious motor coordination deficit was detected. Notably, we observed a robust increase in striatal tyrosine hydroxylase-positive interneurons (THINs). These induced THINs acquire DA-like features by expressing several DA marker proteins (e.g. tyrosine hydroxylase (TH), aromatic L-amino acid decarboxylase (AADC), aldehyde

dehydrogenase 1A1 (ALDH1A1) and Annexin A1 (Anxa1)) in a circuit dependent manner, and exhibit different electrophysiological properties compared to normal striatal TH-positive GABA interneurons, suggesting a local compensatory adaptation to DA loss. iTHINs are not observed in other acute DA lesion PD mouse models, indicating this adaptation is specific due to endocytic defects in DA terminals. Furthermore, acute deletion of SJ1 in adult or aged DA neurons triggers similar DA terminal pathology but with minimal adaptive compensation from iTHINs. Our study not only reinforces the critical role of SJ1 in DA synaptic transmission but also offers insight to striatal adaptive plasticity, which if pharmacologically enhanced, might delay or mitigate PD.

Results

Generation of DA-specific SJ1 conditional knockout (cKO) mice genetically

Given that conventional synaptojanin 1 (SJ1) KO mice exhibit perinatal lethality within 24 hours of birth, we generated SJ1 flx/flx mice by inserting loxP sites flanking exon 4 of *Synj1* gene using CRISPR/Cas9. These mice were then crossed with the DAT-IRES-Cre line to create DA-specific SJ1 conditional KO mice (DAT-Cre;SJ1 flx/flx), hereafter referred to as SJ1 cKO^{DAT} (Fig. 1A).

To confirm successful recombination, we performed immunohistochemistry (IHC) on fixed frozen brain sections using antibodies against SJ1 and DA marker tyrosine hydroxylase (TH) TH. As shown in Fig. 1B and 1C, SJ1 protein expression was significantly reduced in TH-positive DA neurons, reflecting selective depletion in the substantia nigra pars compacta (SNc) and ventral tegmental area (VTA), while SJ1 expression in TH-negative neurons and non-DA brain regions, such as the hippocampus, remained intact. These findings confirm efficient and specific KO of SJ1 in DA neurons. SJ1 cKO^{DAT} mice survived into adulthood without seizures, suggesting that epilepsy reported in SJ1-KI^{RQ} mice and constitutive SJ1 KO mice is likely due to SJ1 loss in other brain regions, such as the hippocampus and cortex(17, 21).

DA Terminal Pathology and DA Deficiency in SJ1 cKO^{DAT} Striatum

To investigate DA-specific pathology in SJ1 cKO^{DAT} mice, we performed IHC for DA-related markers in both midbrain (DA soma) and striatum (DA terminals). In the midbrain,

TH-positive DA neurons appeared morphologically intact, with no significant loss of DA neurons in either the SNc or VTA at 2-3 months old and 6-8 months old (Fig. S1A). However, in the striatum, we observed numerous dopamine transporter (DAT) positive dystrophic clusters in SJ1 cKO^{DAT} but not in the control (Fig. 1D, 1E). Consistent with previous study in SJ1-KI^{RQ} mice (21, 22), this striatal pathology emerged as early as three weeks after birth, progressively increasing in size and number, and peaking at 2–3 months of age (Fig. S1B). However, this pathology was present throughout most of the striatum (Fig. S1C), including the dorsal (both dorsolateral and dorsomedial) and ventral striatum (nucleus accumbens (NAc) core, lateral shell and olfactory tubercle (OT)), with most severe dystrophic changes observed in NAc core region (Fig. S1E). The widespread pathology suggests that the complete loss of SJ1 affects DA terminals from both SNc and VTA DA neurons that innervate the striatum, which is in contrast with SJ1-KI^{RQ} mice (21), where dystrophic DA terminals were primarily restricted to the dorsolateral striatum (nigrostriatal pathway) (Fig. S1D).

There are still DA subpopulations from VTA that show resilience to the complete loss of SJ1. As shown in Fig. S1F-S1H, TH-positive DA fibers in the prefrontal cortex (PFC), basolateral amygdala (BLA) and NAc medial shell (MS), corresponding to the mesocortical pathway (VTA->PFC) and a subset of mesolimbic pathway (VTA->BLA, VTA->NAc-MS), respectively, remained unaffected. Interestingly, DA fibers in these regions were known to have very low or undetectable DAT expression (Fig. S1F, S1H) and unconventional firing property (26), suggesting SJ1 may play an important role for DAT trafficking and function (27), which makes DAT-enriched DA terminals more vulnerable to SJ1 depletion. Together, the comparative results between SJ1-KI^{RQ} and SJ1 cKO^{DAT} mice indicate that the loss of SJ1 in DA neurons is sufficient to cause striatal DA terminal dystrophy in a cell-autonomous and gene-dosage dependent manner.

Further characterization showed that these dystrophic clusters were immunopositive for several other DA markers, including TH, aromatic L-amino acid decarboxylase (AADC), vesicular monoamine transporter 2 (vMAT2), and synaptic vesicle glycoprotein 2C (SV2C) (Fig. 1F, 1G, S2A). While partial colocalization with presynaptic marker, synaptotagmin-1 (Syt1) was observed (Fig. S2B), these dystrophic clusters lacked colocalization with D2 dopamine receptors (D2R), D1 dopamine receptors (D1R), and the medium spiny neuron (MSN) marker Darpp32, indicating that the pathology is restricted to DA terminals (Fig. S2C-S2F).

Immunostaining with astrocyte marker, glial fibrillary acidic protein (GFAP), and microglial marker, ionized calcium-binding adapter molecule (Iba1), did not reveal any obvious gliosis and inflammation in the striatum (Fig. S3A-S3C). We also examined α-synuclein and its pathological form pSer129-α-syn, and observed partial colocalization of DAT-positive dystrophic clusters with α-synuclein (Fig. S3D, S3G). There was no obvious pSer129-α-syn expression observed either in the striatum or midbrain from the control and SJ1 cKO^{DAT} mice (Fig. S3E-S3G).

Interestingly, these clusters were negative for clathrin-dependent endocytic proteins (e.g., SJ1 itself, clathrin light chain, endophilin 1, and amphiphysin 1), suggesting that a clathrin-independent mechanism may contribute to DA terminal dystrophy (Fig. S4A-S4E). Indeed, electron microscopy (EM) of the SJ1 cKO^{DAT} striatum revealed multilayered, whirl-like membrane structures, similar to those previously observed in SJ1-KI^{RQ} and Auxilin-KO mutant mouse models (Fig. 1H) (22). These membrane accumulations correlate with DA marker protein clusters and likely reflect abnormal plasma membrane invaginations at DA terminals. They envelop various organelles, including SVs, mitochondria, autophagosomes, and endo/lysosomes (Fig. 1H, S5A-S5B). Notably, no clathrin-coated vesicles (CCVs) accumulation was observed.

We further performed western blot analysis to assess potential changes in DA-related, synaptic and endocytic protein levels in striatal tissue (Fig. 2A, 2B). The analysis revealed a significant reduction in DAT and vMAT2 levels, while TH, AADC and SV2C levels were not significantly altered, suggesting impaired presynaptic DA transmission in SJ1 cKO^{DAT} mice. The levels of clathrin-associated endocytic proteins—including SJ1, auxilin, BIN1, endophilin 1, dynamin, and AP2, showed no significant changes. Similarly, the level of general synaptic markers such as synapsin, synaptophysin and synaptogyrin 3 were unchanged.

To assess DA metabolism and homeostasis, we conducted high-performance liquid chromatography (HPLC) on striatal extracts from both 2-3 and 6-8 months old SJ1 cKO^{DAT} mice. DA levels were significantly reduced at both time points, whereas DA metabolites, 3,4-dihydroxyphenylacetic acid (DOPAC) (statistically not significant) and homovanillic acid (HVA) levels were elevated (Fig. 2C, 2D). These changes could be a result from impaired SV recycling, reduced vesicular sequestration, and enhanced degradation/oxidation of cytosolic DA.

Following this DA deficiency, we investigated whether SJ1 cKO^{DAT} mice exhibit impaired DA release. To test this, we incubated acute striatal slices with 2 conditions: 40mM potassium chloride (KCl) to depolarize the plasma membrane and evoke vesicular DA exocytosis (Fig. 2E), or with 10 μM amphetamine (AMPH) to induce DA release via DAT-mediated cytosolic DA efflux (Fig. 2F). Under both conditions, DA release was significantly lower in SJ1 cKO^{DAT} mice compared to controls (Fig. 2G, 2H). Reduced KCl-evoked DA release is consistent with the impaired SV recycling and DA package due to reduced vMAT2. Meanwhile, reduced AMPH-induced DA release is likely a result from DAT downregulation, which may limit the action of AMPH, and potentially also from reduced cytosolic DA availability due to accelerated degradation/oxidation.

SJ1 cKO^{DAT} mice Displayed Altered Locomotion without Obvious Motor Coordination Deficits

We next examined how the widespread DA terminal pathology and DA deficiency in the striatum impact the motor function of SJ1 cKO^{DAT} mice. In a 15 min open field test, SJ1 cKO^{DAT} mice showed significant decrease in total distance at both 2-4 and 6-8 months age, suggesting their basal locomotion or exploratory activity is reduced (Fig. 3A, 3B). Given the observed impairment in AMPH-induced DA release in acute striatal slice, we administered AMPH (3mg/kg) and recorded locomotion for 60 min to test for behavioral alterations. Unexpectedly, SJ1 cKO^{DAT} mice displayed significant increase in total traveled distance compared to controls for both 2-4 and 6-8 months age groups (Fig. 3C, 3D). The representative activity trace (Fig. 3E) and the increase in normalized average traveled distance, expressed as percentage of baseline (Fig. 3F, 3G), reflect a markedly heightened response to AMPH treatment. This exaggerated hyperlocomotion in SJ1 cKO^{DAT} mice, despite impaired DA efflux, suggests a dysregulated DA system, likely driven by downstream signaling or receptor sensitivity.

To explore DA receptors' responses, we performed the open field tests on the mice injected with either D1R agonist (SKF81297 2.5mg/kg) or D2R agonist (quinpirole 0.2mg/kg) to activate them respectively. As shown in Fig. 2H-2K, SJ1 cKO^{DAT} mice showed further increased hyperlocomotion after D1R agonist treatment, while the hypolocomotion induced by D2R agonist was comparable to the controls. These results suggest that D1R sensitivity is enhanced in the striatum of SJ1 cKO^{DAT} mice, potentially as a compensatory response to DA deficiency.

To assess specific motor coordination, we performed the rotarod and balance beam tests. Surprisingly, unlike SJ1-KI^{RQ} mice which showed strong motor coordination deficits(21), SJ1 cKO^{DAT} mice performed normally on both tasks (Fig. 3L, 3M). These results indicate either the observed striatal DA terminal pathology is insufficient to impair coordination, or compensatory mechanisms may help maintain motor function.

Locally Adaptive induced TH-positive Interneurons (iTHINs) in SJ1 cKO^{DAT} Striatum

In addition to the TH/DAT-positive dystrophic clusters in DA terminals, there was a striking increase in TH-positive neurons within the striatum of SJ1 cKO^{DAT} mice (Fig. 4A). Striatal TH-positive neurons have been reported in rodents (28-30), primates (31, 32), and humans (33-35). Previous studies using TH-EGFP mice identified them as TH-positive interneurons (THINs), typically undetectable by IHC in wild-type (WT) mice due to low TH expression masked by dense DA axons (36). In SJ1 cKO^{DAT} mice, however, the strong TH protein signal led us to define them as induced TH-positive interneurons (iTHINs). These iTHINs appeared in both dorsal and ventral striatum (Fig. S6A), reaching approximately 200 neurons per coronal section (Fig. 4B). Their emergence paralleled DA terminal dystrophy—first detectable at 3 weeks, peaking at 2–3 months, and persisting into adulthood and aging (Fig. S6B, S6C). Since SJ1 deletion is restricted to midbrain DA neurons, this suggests a robust and sustained local adaptation in the striatum.

In the striatum, 95% of neurons are MSNs. In addition, there are several other striatal interneurons, including neuropeptide Y (NPY), parvalbumin (PV), Calretinin-positive GABA interneurons and choline acetyltransferase (ChAT)-positive cholinergic interneurons(37). To determine the identity of iTHINs, we performed double staining of TH with specific markers for different neuronal types. As shown in Fig. S7A-S7C, iTHINs were not positive for NPY, PV and ChAT, suggesting they represent a distinct subtype of interneurons. We observed few iTHINs occasionally expressed Calretinin or Darpp32 (Fig. S7D, S7E), which is consistent with previous studies and suggest heterogeneity within this population(38, 39). Together, these results further support the specificity of iTHINs induction in response to the loss of SJ1 in DA system**.**

DA-Like Features of iTHINs in SJ1 cKO^{DAT} Striatum

To investigate whether iTHINs adopt DA-like features as a compensatory adaptation, we first assessed their expression of key DA biosynthetic enzymes. Importantly, in addition to TH, which is the first enzyme to convert L-tyrosine to L-DOPA, we observed co-expression of the second enzyme AADC, which further converts L-DOPA to DA. All iTHINs were positive for both TH and AADC, suggesting they possess the molecular machinery for DA synthesis (Fig. 4C).

We next examined the expression of DA transporters: vMAT2 and DAT, which are required for vesicular packaging and reuptake of DA, respectively. Both markers colocalized with TH-positive clusters at dystrophic DA terminals (Fig. 4D) but were absent from iTHINs somata. Using 1.5-fold threshold, the quantification in Fig. 4E showed strong enrichment of AADC in iTHINs, while vMAT2 and DAT expression are below the baseline.

Given the known heterogeneity of striatal THINs (37, 40), we explored whether iTHINs exhibit subregional adaptations linked to specific midbrain DA neuron subtypes. We first examined aldehyde dehydrogenase 1A1 (ALDH1A1), an A9-enriched marker of SNc DA neurons that preferentially innervate the dorsal striatum (Fig. 4F) and represent a population that is particularly vulnerable in PD (41). As expected, ALDH1A1 labelled a DA neuron subtype highly enriched in ventral tier of SNc in both control and SJ1 cKO^{DAT} mice (Fig. S8A). In the striatum, ALDH1A1-positive fibers co-aggregated with TH/DAT-positive clusters in the dorsal region of SJ1 cKO^{DAT} mice (Fig. 4G, S8B), consistent with dystrophic changes in A9-derived terminals. Notably, iTHINs in the dorsal, but not ventral, striatum also expressed ALDH1A1 protein (Fig. 4G, 4H), indicating a spatially restricted acquisition of A9-like features.

We next examined Annexin A1 (Anxa1), a recently identified marker defining a subtype within ALDH1A1-positive SNc DA neurons that projects more selectively to the dorsolateral striatum (Fig. 4I) and is being reported to be highly vulnerable in PD (42-44). Consistent with previous reports (45), Anxa1 immunostaining labelled a subset of of TH (and ALDH1A1)-positive neurons in the ventral SNc (Fig. S8C, S8D). In parallel, only a small subpopulation of iTHINs co-expressed Anxa1, again selectively in the dorsal but not ventral striatum (Fig. 4J, 4K, S8E).

We then checked Calbindin, a marker of A10 VTA DA neurons that mainly projects to ventral striatum (Fig. S8F) (46). While Calbindin labelled a subset of TH-positive neurons in the VTA, it was not detected in any iTHINs in the striatum (Fig. S8G, S8H).

Together, these findings indicate that iTHINs exhibit subregion-specific adaptation, with a dorsal striatal subset acquiring A9/SNc-like molecular features (ALDH1A1 and, in a smaller subset, Anxa1). This spatially patterned signature is consistent with a nigrostriatal circuit-linked response and may reflect a compensatory programme preferentially engaged within dorsal striatal networks most impacted by presynaptic DA dysfunction.

A Second Genetic SJ1 cKO Model (SJ1 cKOTH) Recapitulates DA Terminal Pathology and iTHINs Adaptation

To validate the findings, we generated an independent cell type-specific KO model by crossing SJ1 flx/flx mice with the TH-IRES-Cre line, obtaining SJ1 cKOTH mice (Fig. 5A). While this Cre line also targets TH-positive neurons in other regions (e.g., norepinephrine neurons in the locus coeruleus), our analysis focused on DA neurons in the ventral midbrain and striatum.

As shown in Fig. 5B and 5C, SJ1 was selectively and completely depleted in TH-positive DA neurons of the SNc and VTA. DA terminals in the striatum displayed the same hallmark pathology seen in SJ1 cKO^{DAT} mice—early-onset (1–2 months) dystrophic clusters positive for DA markers including TH, AADC, DAT, vMAT2, and SV2C (Fig. 5D, 5E). These clusters were broadly distributed across the striatum, with ALDH1A1 selectively labelled clusters in the dorsal region (Fig. 5G), further confirming both SNc and VTA DA neurons were affected due to complete loss of SJ1. Importantly, iTHINs were again robustly induced in the striatum, paralleling DA terminal pathology. These iTHINs co-expressed TH and AADC (Fig. 5F), with dorsal striatal subsets also expressing ALDH1A1 (Fig. 5G-5I), indicating their DA-like feature.

Collectively, results from both SJ1 cKO^{DAT} and SJ1 cKOTH mouse models demonstrate that SJ1 loss in DA neurons induces cell-autonomous synaptic pathology, along with the emergence of iTHINs, suggesting a secondary, non-cell-autonomous adaptive response.

Different reporter labelling strategies distinguish iTHINs from WT THINs in SJ1 cKO striatum

To genetically label midbrain DA neurons and striatal THINs, we crossed Ai9 reporter line (Cre-dependent tdTomato (tdT) expression) with both SJ1 cKOTH and SJ1 cKO^{DAT} mice,

generating Ai9;SJ1 cKOTH and Ai9;SJ1 cKO^{DAT} mice (Fig. 6A). As shown in Fig. 6B and 6C, tdT is expressed specifically in TH-positive DA neurons in both control and mutant midbrains.

We next examined the striatum, expecting all TH-positive interneurons to be labelled in TH-Cre dependent manner. As expected, we observed numerous tdT-expressing neurons in the striatum of both Ai9;TH-Cre (control) and Ai9;SJ1 cKOTH mice, representing the total THINs (Fig. 6D). Consistent with prior studies (30), tdT-expressing striatal neurons in Ai9;TH-Cre control mice were not positive for anti-TH antibody staining, implying that they are WT THINs that lacked TH protein (Fig. 6D). In contrast, tdT in Ai9;SJ1 cKOTH striatum labelled two different populations of THINs: approximately 34% of tdT-positive ones are TH immunoreactive positive, representing iTHINs, while about 66% of them were TH immunoreactive negative, which are WT THINs (Fig. 6E). Interestingly, although the soma size of iTHINs is similar to their neighbouring WT THINs (Fig. 6F), the tdT fluorescence intensity is significantly lower in iTHINs (Fig. 6G), suggesting iTHINs may undergo distinct gene/protein expression regulation in response to SJ1 loss.

We further examined the Cre-dependent tdT labeling pattern in the striatum of Ai9;SJ1 cKO^{DAT} mice with its respective control, Ai9;DAT-Cre. In Ai9;DAT-Cre (control) mice, only DA axons were labelled, reflecting that WT THINs do not normally express DAT gene (Fig. 6H). However, in Ai9;SJ1 cKO^{DAT} mice, we unexpectedly observed tdT-expressing neurons in the striatum (Fig. 6H). Importantly, nearly all tdT-expressing neurons were TH immunoreactive positive, suggesting that DAT-Cre dependent tdT expression specifically labelled iTHINs (Fig. 6I). This may be due to activation of the DAT gene in iTHINs, although DAT protein was not detected by immunostaining (Fig. 6H). These findings reinforce the unique DA-like feature of iTHINs compared to WT THINs, and reveal their adaptability to DA neuron dysfunction.

iTHINs exhibit distinct intrinsic electrophysiological properties with reduced excitability compared to WT THINs

To characterize the intrinsic electrophysiological properties of iTHINs and determine how they relate to WT THINs, we performed whole-cell patch-clamp recordings from tdT-positive iTHINs and WT THINs in acute striatal slices of Ai9;SJ1 cKO^{DAT} and Ai9;TH-Cre mice, respectively (Fig. 7A, B).

Consistent with previous reports of THIN (30), WT THINs segregated into three subtypes based on unsupervised clustering of 14 intrinsic membrane properties (Table S1), with principal component analysis (PCA) used for dimensionality reduction and visualization. A three-dimensional scatter plot constructed using representative parameters (e.g., input resistance, action potential half-width, and action potential threshold) revealed clear separation among three WT THINs clusters (Fig 7C, left). In contrast, iTHINs were comparatively homogeneous and occupied a discrete region that did not overlap with WT subtypes, suggesting that iTHINs represent a distinct electrophysiological subpopulation (Fig 7C, right). Consistent with this, unsupervised clustering performed on the combined dataset (WT THINs plus iTHINs) identified four clusters, with iTHINs being significantly enriched in a single cluster (Fig. S9A). To obtain an integrated view of electrophysiological differences among WT THINs and iTHINs, we summarized 14 parameters using normalized population means (Fig. S9B, Table S1). Radar plot analysis revealed distinct parameter profiles across WT THINs clusters and iTHINs, indicating systematic differences in intrinsic states rather than isolated parameter changes (Fig. 7D).

We next compared action potential waveforms by analysing the first evoked spike. iTHINs exhibited spike shapes that differed from WT cluster 1 and cluster 3 neurons, but more closely resembled WT cluster 2 (Fig. 7E), suggesting partial overlap in active membrane properties between iTHINs and this WT cluster 2.

We also assessed excitability using current-clamp recordings during stepwise depolarising current injections (representative traces in Fig. 7F). While all groups displayed features consistent with striatal GABA interneurons reported(36, 37), iTHINs responses were clearly distinct from all three WT THIN subtypes, particularly WT clusters 2 and 3. Notably, WT cluster 2 neurons displayed characteristic prolonged depolarising plateau potentials (PPs) (Fig. 7F, red box). Prior work has shown that DA enhances PPs in WT THINs, while PP duration is reduced in 6-OHDA DA lesion PD model(30, 47, 48). Strikingly, none of the recorded iTHINs exhibited detectable PPs (0/63), consistent with a marked reduction in intrinsic excitability (Fig. 7G). This decrease in iTHIN excitability could contribute to disinhibition of downstream targets, including MSNs (30, 49), potentially as another compensatory adaptation to DA deficiency in the SJ1 cKO striatum. In addition to the absence of PPs, iTHINs showed significantly reduced input resistance, a more hyperpolarised resting membrane potential, and a lack of spontaneous firing (Fig. 7G). Together, these

results indicate a coordinated reduction in intrinsic excitability in iTHINs compared with WT THIN subtypes.

Finally, we also performed whole-cell recordings from labelled SNc and VTA DA neurons in Ai9;DAT-Cre control and SJ1 cKO^{DAT} mice (S10A-E, S10G-K). Relative to controls, only SJ1 cKO SNc DA neurons showed mild changes in several action potential-related parameters, whereas other intrinsic membrane properties were not significantly altered (Fig. S10F, S10L). These data suggest that SJ1 loss primarily affects DA transmission at terminals rather than DA neuron intrinsic properties.

Upregulation of DA markers in iTHINs distinguishes SJ1 cKO from acute DA lesion mouse models

Previous studies using neurotoxin-induced PD rodent and non-human primate models have shown the increase of THINs in the striatum following DA depletion (48, 50-52). To further characterize the iTHINs observed in our genetic SJ1 cKO models, we directly compared them with two acute DA lesion models: (1) the 6-OHDA model and (2) a caspase-3 (Casp3)-mediated ablation model. In the 6-OHDA paradigm, B6 mice received a unilateral injection of the neurotoxin into the midbrain, and brains were collected for IHC analysis two weeks post-injection (Fig. 8A). For the Casp3 lesion model, a Cre-dependent AAV-taCasp3-TEVp was unilaterally injected into the midbrain of DAT-Cre mice, and brain tissue analyzed two weeks post-injection (Fig. 8B). In both models, we observed clear evidence of DA neuron degeneration in the midbrain and a near-complete loss of DA projections in the striatum (Fig. 8C, 8D). Following the depletion of DA fibers, a population of local TH-positive neurons emerged in the striatum (Fig. 8E), consistent with previously reported “THINs” (36). However, compared to the striatum of SJ1 cKO mice, 1) the TH protein expression level is much weaker in these neurons (Fig. 8F); 2) they did not express other DA-related markers, including AADC and ALDH1A1 (Fig. 8G, 8H); 3) they were not labelled by tdT under the Ai9;DAT-Cre background (Fig. S11A), indicating that iTHINs in SJ1 DA cKO striatum acquire more DA-like features. In Table S2, we summarized the differences between iTHINs in SJ1 DA cKO mice and WT THINs from these two acute DA lesion models.

Acute SJ1 KO in Adulthood Triggers Similar DA Terminal Pathology with reduced adaptive Compensation from iTHINs

As described above, iTHINs in genetic SJ1 cKO mice begin to appear at 2-3 weeks of age, peaking at 2-3 months, suggesting that this may be an adaptation during early development stage. To bypass this developmental adaption, we generated acute SJ1 KO mice in DA neurons by unilaterally injecting AAV-TH-Cre virus into the ventral midbrain of adult (2-month) or aged (12-month) SJ1 flx/flx mice (Fig. 9A). To assess the potential non-specific toxic effect of AAV-Cre expression in DA neurons(53, 54), we performed parallel injections in WT mice and found no loss of DA somata or fibers (Fig. S12A, S12B).

At 3-4 months post AAV injection, we confirmed successful acute KO of SJ1, observing efficient depletion of SJ1 in most TH-positive DA neurons on the ipsilateral midbrain (Fig. 9B). Immunostaining results revealed numerous TH/DAT-positive clusters throughout the striatum, resembling the DA terminal pathology observed in genetic SJ1 cKO mice (Fig. 9C, 9D). This confirms the synaptic defects across different DA subpopulations projecting to the striatum due to the complete loss of SJ1. Importantly, even though the number and density of DA terminal clusters were comparable to those observed in genetic SJ1 cKO mice, very few TH-positive iTHINs were detected—about 10% of the number observed in genetic SJ1 cKO mice (Fig. 9E, 9F). Our findings suggest that the secondary compensatory response from iTHINs is primarily induced during early development and gradually diminished during aging. Future longitudinal studies are needed to determine whether acute SJ1 loss leads to progressive DA neurodegeneration and motor deficits via axonal die-back mechanism.

Discussion

In this study, we examined the consequences of SJ1 loss in DA neurons using newly generated DA-specific SJ1 cKO mice. We identified two major cellular outcomes: (1) a primary defect marked by severe dystrophy of DA terminals, with accumulation of DA markers and excess membranes in both dorsal and ventral striatum; and (2) a localized adaptive response involving a robust increase in DA-like striatal TH-positive interneurons (iTHINs) (Fig. S11B). Comparative analysis with WT THINs and acute DA lesion models indicates that iTHINs induction is specific to synaptic endocytic defects in the absence of SJ1. This adaptive striatal plasticity may serve as a neuroprotective mechanism to maintain DA homeostasis or delay terminal degeneration, offering a potential therapeutic strategy to preserve DA function in PD.

Cell-Autonomous, Clathrin-Independent Role of SJ1 in the Neuromodulatory System

SJ1 has been extensively studied in excitatory and inhibitory synapses, where it plays a key role in clathrin uncoating during clathrin-mediated SV endocytosis and recycling. Constitutive whole-body SJ1 KO mice die postnatally with severe epilepsy, suggesting imbalanced excitatory/inhibitory transmission during development(17). While DA-specific SJ1 cKO mice survive to adulthood without seizures, our findings show that striatal DA terminals from both the SNc and VTA undergo significant dystrophic changes, indicating a cell-autonomous role for SJ1 in regulating DA synaptic function. Interestingly, no accumulation of endocytic proteins involved in CME or CCVs were detected in these dystrophic terminals. As neuromodulators, DA neurons release transmitters via "volume transmission", a slower process that does not rely on precise synaptic contact sites(55). This contrasts with the fast "synaptic transmission" seen in excitatory and inhibitory synapses, which primarily recycle SVs through CME. Given these differences, it is plausible that DA synapses utilize alternative mechanisms for SV recycling, such as bulk endocytosis (56).

In addition to DA neurons, another neuromodulatory norepinephrine (NE) neurons are also vulnerable in PD, likely due to shared features such as pace-making firing, extensive axonal arborization, and accumulation of cytosolic oxidized catecholamines. Future studies using our cell type specific SJ1 cKO model could determine whether SJ1 similarly regulates SV recycling in NE neurons and how its dysfunction contributes to their selective degeneration in PD.

Gene Dosage-Dependent SJ1 Loss Correlates with the Severity of DA pathology

There is a clear genotype-phenotype correlation in SJ1-linked PD cases, which is mirrored in mouse models carrying different SJ1 mutations. DA pathology in these models also reflects SJ1 gene dosage. The SJ1-KI^{RQ} model shows selective degeneration of nigrostriatal terminals, while the SJ1 cKO model exhibits more widespread DA terminal dystrophy. This indicates that both A9 and A10 DA neurons are susceptible to impaired SJ1-mediated SV recycling, with A9 SNc neurons being particularly vulnerable, even with partial SJ1 loss. A similar synergistic effect is seen in the Auxilin KO/SJ1-KI^{RQ} double mutant, which displays more severe DA terminal pathology than either single mutant(22). More recently, SJ1 haploinsufficiency has been linked to abnormal mesolimbic signaling and mild motivational deficits(57), suggesting a broader role for SJ1 in VTA DA function that can be further

explored using our SJ1 DA cKO mice. However, we observed a subset of VTA DA neurons in mesocorticolimbic pathways (projecting to PFC, BLA and NAc MS) that are resilient to DA terminal pathology in SJ1 cKO. Interestingly, they all have low level of DAT, the key transporter for DA re-uptake, indicating different DA transmission dynamics may determine their vulnerability. Together, these findings highlight impaired SV recycling as a key driver of DA dysfunction, with partial impairment leading to selective degeneration of SNc DA terminals as a hallmark of PD pathogenesis.

Altered Locomotor Activity but No Obvious Coordination Deficits in SJ1 DA cKO mice

Along with severe DA terminal pathology, the striatum of SJ1 cKO mice showed reduced DA content, increased breakdown, and impaired DA release/efflux. The reduced spontaneous locomotion in the open field likely reflects this diminished DA tone. However, the exaggerated hyperlocomotion after AMPH treatment, despite having blunted AMPH-induced DA efflux, points to compensatory postsynaptic hypersensitivity. Consistently, SJ1 cKO mice exhibited a significant increase in locomotion after D1R, but not D2R agonist treatment, suggesting the hypersensitization of DA receptors in the striatum.

Surprisingly, SJ1 cKO mice displayed intact motor coordination in rotarod and balance beam tests, despite showing more severe pathology than SJ1-KI^{RQ} mice. This preservation suggests several possibilities: (1) motor symptoms in SJ1-KI^{RQ} mice may arise from combined SJ1 dysfunction across multiple brain regions, not just DA neurons; (2) DA terminal dystrophy observed in SJ1 mutant mice may represent a prodromal phase of PD that does not progress to full clinical manifestations within the mouse lifespan; and (3) local compensatory mechanisms within the striatum may preserve basic motor coordination despite significant synaptic dysfunction.

Our findings align with recent studies using DA-specific cKO mouse models of two important synaptic transmission proteins: the Ca^{2+} sensor Syt1 and the release site organizer RIM1/2(58, 59). In both cKO models, although activity- or action potential-induced phasic DA release is significantly abolished, the mice do not exhibit obvious motor defects(58, 59). Furthermore, early compensatory changes, such as receptor adaptation and enhanced DA synthesis, packaging, and innervation, have been observed in the striatum of Syt1 DA-cKO mice(58). These results suggest that DA-dependent motor functions can be sustained by basal extracellular DA levels and striatal compensatory plasticity.

Taken together, the converging results from three DA-specific cKO models with impaired synaptic transmission support the idea that strong motor coordination deficits of PD only emerge after extensive DA denervation. These models may therefore capture key aspects of the pre-symptomatic or early compensatory stages of PD, where functional abnormalities in DA terminals are present, but motor coordination remain intact.

Adaptive Compensation of iTHINs in SJ1 DA cKO Striatum

A prominent adaptive change in the striatum of SJ1 DA cKO mice is the robust increase of iTHINs. A much milder induction of iTHINs was also observed in SJ1-KI^{RQ} and Auxilin KO/SJ1-KI^{RQ} double mutants, suggesting that this response is specific to endocytic defects and modulated by gene dosage(22).

Neurotoxin-induced PD models (6-OHDA, MPTP) in rodents and non-human primates have shown increased THINs in the striatum following DA depletion, suggesting a potential compensatory or protective role(48, 50-52). However, it has been debatable whether these THINs qualify as bona fide DA neurons capable of expressing key DA markers (e.g., AADC, DAT) and producing/releasing DA(36, 52, 60).

In our study, when compared with acute 6-OHDA and Casp3 lesion models, iTHINs in SJ1 cKO mice displayed distinct DA-like features: strong co-expression of TH and AADC, and the expression of the SNc DA neuron marker, ALDH1A1 and Anxa1 in a subset of dorsal striatal iTHINs, indicating a region-specific and circuit-dependent compensatory response to DA terminal degeneration. While SV-related markers like vMAT2 were not detected, it's worth noting that non-vesicle mediated somato-dendritic DA release in the midbrain has been proposed previously(61). Future biochemical and physiological studies are needed to determine iTHINs capacity for DA production and release. Alternatively, iTHINs may retain their GABAergic interneuron identity but reduce its excitability, as indicated by our whole-cell patch-clamp recordings. iTHINs may therefore contribute to striatal DA homeostasis through two complementary mechanisms: (1) adopting DA-like features to partially compensate for presynaptic DA deficiency, and (2) reshaping local circuit by reducing inhibitory interneuron output and thereby disinhibiting postsynaptic striatal targets, which could enhance downstream DA signalling(36).

A key open question is what signal striatal THINs detect to initiate their induction. While extracellular DA levels were previously shown to negatively regulate THINs number(62), intriguingly, acute DA lesion models with severe DA depletion do not induce iTHINs. This indicates that other factors—likely released from DA fibers—are required to initiate and sustain DA-like features in iTHINs.

Moreover, as THINs form connections with other striatal neurons(30, 37), and actively engage in local crosstalk, advanced approaches including single-nucleus RNA sequencing and spatial transcriptomics could be employed to further study the molecular identity and functional role of iTHINs in striatal microcircuits. By elucidating these mechanisms of striatal plasticity, we can open new paths for therapeutic strategies that target circuit-level compensation in PD.

Methods

Sex as a biological variable

Sex was not treated as a biological variable, both male and female mice were included.

Animals

Mice were housed in SPF rooms with a 12-hour light/dark cycle. SJ1-KI^{RQ} mouse line was generated as described before and a gift from Prof Pietro De Camili (Yale University)(21). SJ1 flx/flx (C57BL/6J-Synj1^{em1cyagen}; S-CKO-00357, Cyagen) was generated by inserting loxP sites flanking exon 4 of Synj1 using CRISPR/Cas9. These mice were crossed with DAT-IRES-Cre (C001024, Cyagen) and TH-IRES-Cre knock in line (EM:00254, European Mouse Mutant Archive; kindly provided by Dr Sarah Luo, IMCB-A*STAR) to obtain double heterozygous, +/DAT-Cre;SJ1 +/flx and +/TH-Cre;SJ1 +/flx mice, respectively. To create DA-specific SJ1 conditional KO mice, double heterozygous mice were crossed with homozygous SJ1 flx/flx, obtaining +/DAT-Cre;SJ1 flx/flx and +/TH-Cre; SJ1 flx/flx mice, referred to as SJ1 cKO^{DAT} and SJ1 cKOTH, respectively. Appropriate littermate or age-matched controls (SJ1 flx/flx or +/DAT-Cre;SJ1 +/flx or +/TH-Cre;SJ1 +/flx) were used in all experiments. All mice used in the experiments with Cre-dependant promoter were heterozygous, simply referred as DAT-Cre and TH-Cre in the manuscript.

Ai9 mice (B6.Cg-Gt(ROSA)26Sortm9(CAG-tdTomato)Hze/J; RRID: IMSR_JAX:007909) were kindly provided by Prof Enrico Petretto (Duke-NUS) for specific labelling following Cre-mediated recombination. Homozygous Ai9 mice were first crossed with homozygous SJ1 flx/flx to obtain double heterozygous, +/Ai9;SJ1 +/flx mice. Subsequent models involving Ai9 were all heterozygous Ai9, hence simply referred as Ai9 in the manuscript. Ai9;SJ1 +/flx mice were then crossed with SJ1 cKO^{DAT} and SJ1 cKO^{TH} to obtain Ai9;SJ1 cKO^{DAT} and Ai9;SJ1 cKO^{TH}, respectively. Appropriate littermate or age-matched controls were used in all experiments.

For SJ1 acute KO mouse model, SJ1 flx/flx mice were employed. Briefly, mice were stereotactic injected AAV.rTH.PI.Cre.SV40 (1ul) (Addgene-#107788) unilaterally in right midbrain (AP 3.3 mm, ML 1.2 mm, DV 4.3 mm) after anesthetized by isoflurane (5% induction, 2% maintenance at 0.5-0.8 L/min oxygen or air flow). Mice brain tissues were harvested for IHC at 3-4 months post injection.

For 6-hydroxydopamine (6-OHDA; H4381, Sigma-Aldrich) lesion model, B6 mice (C57BL/6J; RRID:IMSR_JAX:000664**)** were treated with desipramine (D3900, Sigma-Aldrich; i.p. 25 mg/kg) 30 min prior to 6-OHDA infusions to prevent noradrenergic neurons. 6-OHDA (2.88 ug, dissolved in 0.2% ascorbate/saline solution) was unilaterally pressure injected into the right midbrain (AP 3.3 mm, ML 1.2 mm, DV 4.3 mm). Mice brain tissues were harvested for IHC at 2 weeks post 6-OHDA injection.

For Casp3 ablation model, Cre-dependent virus, pAAV-flex-taCasp3-TEVp (1ul) (Addgene-#45580) were unilaterally injected in Cre heterozygous mice right midbrain (AP 3.3 mm, ML 1.2 mm, DV 4.3 mm) after anesthetizing. Mice brain tissues were harvested for IHC at 2 weeks post injection.

Antibodies

The antibodies used in this study were obtained from commercial sources as stated: mouse anti-α-synuclein (610786, RRID: AB_398107), mouse anti-AP2 (611350, RRID: AB_398872) and mouse anti-Dynamin (610245, RRID: AB_397640) from BD Biosciences; goat anti-ChAT (AB144P, RRID: AB_2079751), mouse anti-clathrin light chain (AB9884, RRID: AB_992745), rat anti-DAT (MAB369, RRID: AB_2190413), mouse anti-SV2C (MABN367, RRID: AB_2905667) and rabbit anti-TH (AB152, RRID: AB_390204) from Merck Millipore;

mouse anti-β-actin (sc-47778, RRID: AB_2714189) and mouse anti-BIN1 99D (sc-13575, RRID:AB_626753) from Santa Cruz Biotechnology; rabbit anti-ALDH1A1 (HPA002123, RRID: AB_1844722), rabbit anti-GFAP (ZRB2383, RRID: AB_2905668) and rabbit anti-SJ1 (HPA011916, RRID: AB_1857692) from Sigma-Aldrich; rabbit anti-Endophilin 1 (159002, RID: AB_887757), mouse-anti Calretinin (214111, RRID: AB_2619904), mouse anti-TH (213211, RRID: AB_2636901), rabbit anti-Amphiphysin 1 (120002, RRID: AB_887690), rabbit anti-Synaptogyrin 3 (103302, RRID:AB_2619752), rabbit-anti Synaptophysin 1 (101002, RRID:AB_887905), rabbit anti-AADC (369003, RRID: AB_2620131), guinea pig-anti Calbindin D28k (214005, RRID: AB_2619902), mouse anti-Parvalbumin (195011, RRID: AB_2619883) and rabbit anti-D2R (376 203, RRID: AB_2636918) from Synaptic Systems; rabbit anti-vMAT2 (MSFR106400, RRID: AB_2571857) from Nittobo Medical; rabbit anti-DARPP-32 (2306, RRID: AB_823479) and rabbit anti-Neuropeptide Y (11976, RRID: AB_2716286) from Cell Signaling Technology; rabbit anti-Iba1 (019-19741, RRID: AB_839504) from FUJIFILM Wako Pure Chemical Corporation; goat anti-ALDH1A1 (AF5869_RRID: AB_2044597) from R&D Systems; rabbit anti-alpha synuclein phospho S129 (EP1536Y, RRID:AB_765074) from abcam; rabbit anti-DRD1 (17934-1-AP, RRID:AB_10598308), mouse anti-GAPDH (60004-1, RRID: AB_2107436) and rabbit anti-GAPDH (10494-1-AP, RRID: AB_2263076) from Proteintech; rabbit anti-Annexin A1 (71-3400, RRID:AB_88080) from Thermofisher.

The rabbit anti-Synapsin was obtained from Prof Pietro De Camilli's lab at Yale University.

Secondary antibodies used were all purchased from commercial sources as stated: donkey anti-mouse IgG (H□+□L) Alexa Fluor Plus 488 (A32766, RRID: AB_2762823), donkey anti-mouse IgG (H□+□L) Alexa Fluor 594 (A21203, RRID: AB_2535789), donkey anti-mouse IgG (H□+□L) Alexa Fluor Plus 647 (A32787, RRID: AB_2762830), donkey anti-rabbit IgG (H□+□L) Alexa Fluor Plus 488 (A32790, RRID: AB_2762833), donkey anti-rabbit IgG (H□+□L) Alexa Fluor Plus 594 (A32754, RRID: AB_2762827), donkey anti-rabbit IgG (H□+□L) Alexa Fluor 647 (A32795, RRID: AB_2762835), donkey anti-rat IgG (H□+□L) Alexa Fluor Plus 488 (A48269, RRID: AB_2893137), donkey anti-rat IgG (H□+□L) Alexa Fluor 594 (A21209, RRID: AB_2535795), donkey anti-goat IgG (H□+□L) Alexa Fluor 488 (A11055, RRID: AB_2534102), donkey anti-goat IgG (H□+□L) Alexa Fluor 594 (A32758, RRID: AB_2762828), goat anti-guinea pig IgG (H□+□L) Alexa Fluor 488 (A11073, RRID: AB_2534117) and goat anti-guinea pig IgG (H□+□L) Alexa Fluor 647 (A21450, RRID: AB_2535867) from Life Technologies; goat anti-mouse IgG light chain

HRP (AP200P, RRID:AB_805324) and mouse anti-rabbit IgG light chain HRP (MAB201P, RRID:AB_827270) from Merck; IRDye 800CW donkey anti-rabbit IgG (926-32213, RRID: AB_621848), IRDye 800CW donkey anti-mouse IgG (926-32212, RRID: AB_621847), IRDye 680RD donkey anti-mouse IgG (926-68072, RRID: AB_10953628) and IRDye 800CW goat anti-rat (926-32219, RRID: AB_1850025) from LI-COR Biosciences.

Brain Histology and Immunofluorescence

Mice were anesthetized with a Ketamin/Xylazine anesthetic cocktail injection, perfused transcardially with ice-cold 4% paraformaldehyde in 1 X phosphate-buffered saline (PBS) and the brains were kept in the same fixative overnight at 4°C. On the next day, brains were transferred to 30% sucrose in 1 X PBS and kept overnight at 4°C on top of a roller. Brains were then embedded in OCT (Tissue-Tek) and freeze in liquid nitrogen-cooled 2-methylbutane (Isopentane). Coronal or sagittal sections of 20 µm thickness were cut with a cryostat. The sections were either mounted on adhesive slide, SuperFrost® Plus (VWR) or collected as floating sections in 1 X PBS in a 24-well plate. Sections were then blocked in 5% BSA and 0.1% Triton X-100 in 1 X PBS for 1 hour at room temperature. After blocking, sections were incubated with primary antibodies and kept overnight at 4°C. Subsequently, sections were washed 3 times for 10 min with 0.1% Triton X-100 in 1 X PBS, then incubated with Alexa-conjugated secondary antibodies for 1 hour at room temperature. Finally, the sections were mounted with Fluoromount-G (Invitrogen) and sealed with nail polish. The floating sections were mounted onto slides after all the staining procedures. Images were acquired with Andor BC43 (Oxford Instruments) with 10x, 20x and 40x oil objective or a spinning disk system (Gataca Systems) based on an inverted microscope (Nikon Ti2-E; Nikon) equipped with a confocal spinning head (CSU-W, Yokogawa) and a Plan-Apo 20x and 40x oil objective.

For stereological analysis of TH-positive DA neurons in the midbrain, 30 µm coronal section were collected incubated with 0.1% H2O2 for 5 min to quench endogenous peroxidase activity and subsequently incubated with buffer containing 5% BSA, and 0.1% Triton X-100 in 1X PBS for 1 hour at room temperature. Next, sections were incubated overnight at 4°C with anti-TH primary antibody (1:1000). The sections were then washed with 1X PBS three times for 10 min and incubated with a biotinylated anti-rabbit secondary antibody (Vector Laboratories, USA) for 1 hour at room temperature, later followed by incubation with

Avidin/Biotin complex (ABC) reagent (Vector Laboratories, USA) at room temperature. Finally, immunoreactivity was revealed by incubation with diaminobenzidine (DAB). Stereological analysis was performed using the optical fractionator probe in the Stereo Investigator (MBF Bioscience) software. A total of 7-9 coronal sections of every fourth sections were collected across the midbrain and used for counting. The SNc and VTA regions were outlined based on the Allen mouse brain atlas and counting was performed using 63x oil lens. The parameters used were guard zone of 2 μm, dissector height of 13 μm and counting frame of 200 μm x 200 μm.

Quantitative Image Analysis

All quantitative analyses were performed using Fiji software (Version ImageJ 2.160/1.54p/Java 1.8.0_322 (64-bit), RRID: SCR_002285). Image acquisition parameters were kept constant for experimental groups.

Quantification of SJ1 Expression in DA Neurons

TH-positive neurons were identified by manual intensity thresholding of the TH channel followed by size filtering to exclude particles smaller than 60 μm^2, generating neuronal ROIs. These ROIs were applied to the SJ1 channel after background subtraction. Mean fluorescence intensity of SJ1 within TH-positive ROIs was quantified and averaged per animal to yield a single mean intensity for the SNc and VTA. For each experiment, control values were normalized to 100%, and SJ1 cKO values were expressed relative to this control mean.

Quantification of DAT Immunoreactivity Clusters

For each mouse, 5 random sampling sites were selected respectively for both dorsal and ventral striatum. At least three mice from each genotype and each age group were collected for this purpose. The threshold setting for the clusters was set to quantify puncta bigger than 5 μm^2 to ensure normal positive axonal terminals were not counted in. The average size of clusters and average number of clusters was counted automatically with Fiji plugin “Analyse Particles” based on all five random sampling sites for each mouse. Density of clusters was calculated as the number of clusters per ROI area and normalized to a standard 300 × 300 μm^2 area.

Colocalization Analysis

Colocalization between different markers was assessed using Pearson's correlation coefficient (PCC). PCC values were calculated using the JaCoP plugin in Fiji. Mean PCC values were obtained from 3–7 sections per animal and averaged for statistical analysis.

Glia Quantification

Iba1-positive microglial and GFAP-positive astrocytic area fractions were quantified in striatal sections using custom macros implemented in Fiji and executed in batch mode. Images were first converted to 8-bit grayscale and median-filtered (radius = 1 pixel) to reduce background noise while preserving cellular morphology. Binary masks were generated by automated thresholding using the *Triangle* method for Iba1-stained images and the *Yen* method for GFAP-stained images. Following thresholding, despeckling was applied to remove isolated noise artifacts. The percentage area fraction of positive staining was then calculated from the resulting binary masks.

Enrichment ratio

Striatal TH-positive neurons (iTHINs) were identified by manual intensity thresholding of the TH channel in the striatum image, generating neuronal ROIs. For each channel of the protein interest, the mean fluorescence intensity within every iTHINs ROI was measured. In the same field, 1-3 ROIs were manually drawn in the background fibers to obtain an average mean intensity for normalization. Data was collected from 1-3 random ROIs from coronal striatum image. The enrichment ratio for each TH ROI was calculated as: Mean intensity in TH ROIs / Mean intensity of background fibers. Protein expression in the TH ROIs was classified as "enriched" when it is above 1.5.

Quantification of TH-positive Striatal Interneurons

Quantification of TH-positive and tdT-expressing cells was conducted using Fiji software (Version ImageJ 2.160/1.54p/Java 1.8.0_322 (64-bit), RRID: SCR_002285) with full stitched half coronal section. Image acquisition involved tiling of the entire section with either 10x or 20x objective lens on Andor BC43. Cell Counter plugin in Fiji software was used to count visible cell bodies across the striatum (outlined based on Allen mouse brain atlas). Cell count from individual channels was used for percentage ratio quantification.

Quantification for TH-positive cells intensity in lesioned and genetic mouse models was done using Fiji software. A consistent threshold was applied across all images to isolate TH-positive signals. The 8-bit figure type was used to measure the mean density of the TH signal. Background fluorescence was determined from adjacent areas without specific staining. All measurements were performed under identical settings to ensure consistency across experimental groups. For each mouse, 6 random TH-positive cells were selected from both dorsal and ventral striatum. At least three mice from each condition were collected for this purpose.

Quantification for tdT expression in Ai9;SJ1 cKOTH mouse model for WT THINs and iTHINs was quantified from stitched coronal striatum images. Cells were classified as either tdT-positive only or tdT/TH double-positive based on TH immunoreactivity. For each animal, five random regions of interest (ROIs) containing tdT signal were selected from the stitched image for analysis. Cells were identified by manual intensity thresholding of the tdT channel followed by size filtering to exclude particles smaller than 60 μm², generating neuronal ROIs. Mean fluorescence intensity of tdT within ROIs was quantified and averaged per animal to yield a single mean intensity. Fluorescence intensity was measured in Fiji using corrected total cell fluorescence (CTCF), calculated as integrated density minus the product of cell area and mean background fluorescence. Background fluorescence was measured from a cell-free area within the same stitched image, and the same background value was applied to all cells quantified from that stitched image. A total of four mice were used for quantification.

Long soma diameter for WT THINs and iTHINs was quantified in the same brain sections collected from Ai9;SJ1 cKOTH mouse model. Using the same ROIs above, the diameter of each cell was measured in Fiji by tracing the longest axis of the soma. For statistical analysis, individual cell measurements were averaged per mouse, and the mean long soma diameter for each subpopulation was calculated. At least three mice were used for this quantification.

Electron Microscopy

2 months old mouse was anesthetized and fixed by transcardial perfusion with 4% paraformaldehyde and 0.125% glutaraldehyde (EMS, Hatfield, PA) in 0.1 M PB buffer. Brain was removed and dissected in small pieces (1 × 1 × 1 mm^3) and further incubated in 2.5% glutaraldehyde in 0.1 M PB buffer at 4 °C overnight. The samples were then washed for 5 min in 1 X PBS for three times. The samples were post-fixed with 1%

osmium tetroxide for 1 hour and washed with distilled water. They are then dehydrated through an ethanol series (25%, 50%, 75%, 95% and 100%) and absolute acetone, before infiltrating with araldite resin/acetone mixtures. On the next day, samples were further infiltrated in pure resin at 40°C to 50°C, then embedded in resin and polymerised at 60°C for 24 hours. The embedded sample was sectioned into 100nm slices with a Leica UC6 ultramicrotome and stained with lead citrate. Images were captured with JEOL JEM-1400Flash TEM, operating at 100kV.

Immunoblotting

Striatum tissues were homogenized in buffer containing 20 mM Tris-HCl (pH 7.4), 150 mM NaCl, 2 mM EDTA and cOmpleteTM EDTA-free Protease Inhibitor Cocktail (Roche, USA). The homogenized samples were centrifuged at 700 g for 10 min to obtain the post-nuclear supernatant (PNS). Protein concentration was determined by the Pierce BCA Protein Assay Kit. SDS-PAGE and western blotting were performed by standard procedures. The membranes were blotted with primary antibodies and then IRDye® Secondary Antibodies (LI-COR, USA) or HRP light chain secondary antibodies. The protein bands were detected using Odyssey ® CLx imaging system or Bio-Rad ChemiDoc Touch Imaging System, and its intensity was quantified via Image Studio. A minimum of three independent sets of samples were used for quantification.

HPLC

Striatum tissues dissected from mice brain were homogenized in 0.5 N perchloric acid with 100 µM of deferoxamine mesylate and 100 µM of glutathione. The homogenized samples were further sonicated, centrifuged and the supernatants were filtered using 0.1 µm PVDF centrifugal filters before collecting the filtrates for HPLC analysis. A reversed-phase UltiMate 3000 HPLC system (Thermo Fisher Scientific) with an electrochemical detector and a reversed-phase column (Vydac Denali, C18, 4.6 x 250 mm, 5 µm particle size, 120 Å pore size) were used to run the samples. The HPLC run was performed at a flow rate of 1 ml per minute with a mobile phase containing 1.3% sodium acetate, 0.01% EDTA (pH8.0), 0.5% sodium 1-heptanesulfonate, 7% acetonitrile (v/v) and 2% methanol (v/v), adjusted to pH 4.0 with acetic acid. All buffers used for HPLC analysis were double filtered through 0.2 µM

nylon membranes. Dopamine, DOPAC and HVA levels in the samples was identified by retention time of their respective standard and quantified by measuring the area under the peak using the software ChromeleonTM 7.2 Chromatography Data System (Thermo Fisher Scientific). The areas under the peaks were normalized to their respective tissue weight.

Acute Brain Slice Preparation

Mouse brains were rapidly removed after decapitation and placed in high-sucrose ice-cold oxygenated artificial cerebrospinal fluid (ACSF) containing the following (in mM): 125 NaCl, 25 $NaHCO_3$, 10 glucose, 2.5 KCl, 2.5 $MgCl_2$, 0.5 $CaCl_2$, 1.24 NaH_2PO_4, 1.68 HEPES, pH 7.4 and 95% O_2/5% CO_2. Coronal brain slices were cut at a thickness of 250 μm using a vibratome (VT1200S, Leica Biosystems) and immediately transferred to an incubation chamber filled with ACSF containing the following (in mM): 125 NaCl, 25 $NaHCO_3$, 10 glucose, 2.5 KCl, 2 $MgCl_2$, 1 $CaCl_2$, 1.24 NaH_2PO_4, 1.68 HEPES, pH 7.4 (300–310 mOsm), equilibrated with 95% O_2 and 5% CO_2. Slices were allowed to recover at room temperature at least for 60 min.

For KCl-evoked and AMPH-induced release, striatum brain slices were incubated with 300 μL pre-warmed ACSF containing the following (in mM): 125 NaCl, 25 $NaHCO_3$, 1.25 $NaH_2PO_4.2H_2O$, 2.5 KCl, 1.8 $CaCl_2$, 1 $MgCl_2$, 0.4 ascorbic acid, pH 7.4 (300–310 mOsm) at 37 °C, 5 min. The incubation medium in this step served as the baseline control for subsequent measurements. Another 300μL ACSF containing 40 mM KCl or 10 μM amphetamine (AMPH; d-(+)-Amphetamine sulfate, D961, Age D'or) were added to incubated with the same striatum brain slices at 37 °C, 5 min. The incubation medium in this step served as the KCl-evoked or AMPH-induced DA released samples from striatum of control (DAT-Cre;SJ1 +/flx) and SJ1 cKO^{DAT} mice for subsequent HPLC detecting. After adjusting the final concentration of the ACSF buffer to 0.1 N perchloric acid, the DA released samples was filtered through 0.1 μm PVDF centrifugal filters and subjected to HPLC analysis using the same parameters as those used for striatum tissues detection. The areas under the peaks were normalized to their respective protein concentration.

Motor Behavioral Tests

SJ1 cKO^{DAT} and mice between 2-8 months old were used for balance beam and rotarod tests. The mice were divided into two age groups: 2-3 months old (n= 13 for Ctrl, n=15 for SJ1 cKO^{DAT}) and 6-8 months old (n=9 for Ctrl and n=10 for SJ1 cKO^{DAT}). Both males and females were used for the behavioral assays. Both tests were conducted during the light period. The mice were allowed to be acclimatized to the test for at least 30 min before each test.

Balance Beam Test

A narrow beam (10 mm width) was suspended 15 cm above a soft padding. Mice were placed on end of the beam and during their trip towards the other end, the number of missteps (paw slips) was recorded. The test was conducted thrice for each mouse, and the average number of missteps was calculated.

Rotarod Test

Mice were placed on a rod which is rotating at 4 rpm with an acceleration to 40 rpm within 6 min. The duration of the mice staying on the rod is measured three times at 10 min intervals and the average 'latency to fall' was determined for each mouse.

Open Field Test (OFT)

Mice were placed in a chamber measured 40 cm (length) x 40 cm (width) x 30 cm (height) and recorded for 15 min. Recorded videos were analyzed with TopScan video tracking software. The mice path tracking and time spent in the defined area were analyzed. The mice used for two age groups: 2-3 months old (n= 7) and 6-8 months old (n= 6), unless otherwise stated.

For drug treatment open field test, after 15 min baseline recording, intraperitoneal injections of amphetamine at 3.0 mg/kg (D961, Age D'or) or SKF81297 at 2.5mg/kg (S143, Sigma-Aldrich) or quinpirole at 0.2mg/kg (sc-253339, Santa Cruz) were administered, dosage was optimized with reference to literature(58). Total traveled distance of the mice after 60 min injection was recorded by the tracking system and the results were normalized to individual baseline. Traveled distance was expressed by percent of baseline. Percent of baseline was calculated per animal as (post_mean / baseline_mean) × 100, where baseline_mean is the mean distance over the 15-min pre-drug period and post_mean is the mean distance over the 60 min post-drug test.

Electrophysiology

Brain slice preparation

Mouse brains were rapidly removed after decapitation and placed in high-sucrose ice-cold oxygenated artificial cerebrospinal fluid (ACSF) containing the following (in mM): 250 sucrose, 26 $NaHCO_3$, 10 glucose, 2.5 KCl, 4 $MgCl_2$, 0.1 $CaCl_2$, 1.25 $NaH_2PO_4.2H_2O$, 3 Myo-Inositol, 2 Na-pyruvate, 0.5 ascorbic acid,1 kyneurenic acid, pH 7.4 and 95% O2/5% CO_2. Coronal brain slices were cut at a thickness of 250 µm using a vibratome (VT1200S, Leica Biosystems) and immediately transferred to an incubation chamber filled with ACSF containing the following (in mM): 125 NaCl, 25 $NaHCO_3$, 1.25 $NaH_2PO_4.2H_2O$, 2.5 KCl, 1.8 $CaCl_2$, 1 $MgCl_2$, pH 7.4 (300–310 mOsm), equilibrated with 95% O2 and 5% CO_2. Slices were allowed to recover at 32 °C for 30 min and then maintained at room temperature.

Whole-cell patch-clamp recordings and data analysis

The neurons were recorded with the internal solution (pipette solution) containing (in mM) 130 K-gluconate, 10 KCl, 5 EGTA, 10 HEPES, 1 $MgCl_2$, 0.5 Na_3GTP, 4 Mg-ATP, 10 Na-phoshocreatine pH 7.4 (adjusted with KOH) and external solution containing (in mM): 10 glucose, 125 NaCl, 25 $NaHCO_3$, 1.25 $NaH_2PO4.2H_2O$, 2.5 KCl, 1.8 $CaCl_2$, 1 $MgCl_2$, pH 7.4 (300–310 mOsm), equilibrated with 95% O2 and 5% CO_2.Whole cell recording are performed with multi-clamp 700b amplifier (Molecular Device), low-pass filtered at 1 kHz and the series resistance was typically <20 MΩ after >50% compensation. Cell-attached recordings for SNc and VTA neurons were performed before break-in with 0 mV holding. Current clamp recordings for spontaneous firing were performed with 0 pA current injection. To evoke action potential firing, SNc neurons were first held with 0 pA current holding followed by injection of increasingly positive current injection from -80 pA to 110 pA with 10 pA increment. VTA neurons were first held with 0 pA current holding followed by injection of increasingly positive current injection from -50 pA to 140 pA with 10 pA increment. Striatal neurons were first held with 0 pA current holding followed by injection of increasingly positive current injection from -100 pA to 280 pA with 20 pA increment. Data was analyzed with Clampfit 11.4.2 and Prism.

Intrinsic electrophysiological properties were extracted as previously described(30, 37, 40, 47). A total of 14 parameters were quantified for striatal THINs, whereas 12 parameters were extracted for midbrain DA neurons, reflecting cell type–specific electrophysiological features.

For striatal TH-positive neurons (WT THINs and iTHINs), the extracted parameters included: maximal firing frequency, input resistance, resting membrane potential (RMP), action potential (AP) threshold, AP width at 50% relative to baseline and threshold, AP amplitude relative to baseline and threshold, after-hyperpolarization (AHP) amplitude, spontaneous activity, plateau potential duration, low-threshold spike (LTS) component, hyperpolarization-activated current (Ih ratio), and membrane capacitance.

For midbrain DA neurons, parameters included: maximal firing frequency, input resistance, AP threshold, AP width at 50% relative to baseline and threshold, AP amplitude relative to baseline and threshold, AHP amplitude, cell-attached firing frequency, break-in firing frequency, Ih ratio, and membrane capacitance.

For population-level analysis of striatal THINs, extracted intrinsic electrophysiological parameters were compiled into feature matrices and subjected to dimensionality reduction and clustering. Analyses were first performed on wild-type (WT) THINs to define baseline electrophysiological subtypes, followed by analysis of WT–iTHINs combined datasets using the same analytical framework to enable direct comparative mapping between conditions. This framework enabled unbiased identification of electrophysiologically distinct neuronal subtypes and quantitative assessment of genotype-dependent shifts in intrinsic neuronal properties.

Principal component analysis (PCA) was performed using singular value decomposition implemented in the pcaMethods package in R, with mean centering and unit variance scaling. Principal component scores were extracted, and components capturing the majority of variance were used for downstream clustering. Unsupervised hierarchical clustering was performed using Euclidean distance and Ward’s minimum variance method (ward.D2). The optimal number of clusters was determined by silhouette analysis using the cluster package.

For visualization, three electrophysiological parameters with the greatest discriminatory power between clusters were selected to generate three-dimensional feature-space representations. These were constructed in three configurations: WT clusters alone, iTHINs projected onto WT-defined clusters, and combined clustering of WT THINs and iTHINs.

Radar plots were generated following feature-wise normalization to a 0–1 range to compare averaged electrophysiological profiles across clusters and conditions.

All statistical analyses and data visualization were performed in R using standard packages, including pheatmap, FactoMineR, ggplot2, and related libraries.

Statistical Analysis

All statistical analysis was performed using GraphPad Prism (Ver 10.6.1, RRID: SCR_002798) otherwise stated. All graphs were plotted on GraphPad Prism otherwise stated. Data are presented as mean ± SEM unless otherwise stated. Comparisons between two independent groups were conducted using Welch's unpaired t-test. For analyses involving more than two groups, one-way or two-way ANOVA with Tukey's honestly significant difference (HSD) post hoc test was applied. For repeated measures data from the 60 min open field test, two-way ANOVA with Tukey's HSD post hoc test was performed. For normally distributed datasets from electrophysiology experiments, significance analysis was performed using unpaired Student's t-tests (two-tailed) or ANOVA, followed by Tukey's post-hoc test. For non-normally distributed datasets, Mann-Whitney U tests or Kruskal-Wallis tests were used, with Dunn correction for multiple comparisons. Data with p-values <0.05, <0.01, <0.001, and <0.0001 are represented by asterisks *, **, ***, and ****.

Study Approval

All experiments involving animals were conducted according to the protocol approved by SingHealth Institutional Animal Care and Use Committee (IACUC).

Data Availability

The datasets generated and/or analyzed in this study are available from the corresponding author Mian Cao on request. All other data needed to evaluate the conclusions in the paper are present in the paper and/or the Supplementary Materials.

Author Contributions

Y.L., Z.L., B.M., M.L., and M.C. designed the experiments. Y.L., M.L. and Z.L. performed sample preparations, histology experiments and microscopy imaging. Y.L. and X.C performed HPLC and analysis. Y.L. performed western blotting and analysis. M.L. performed stereological quantification. Y.L. and M.C. performed sample preparations for EM. Y.L., B.M., M.L., X.C. and Z.W. performed behavioural experiments. Z.L. B.M., and M.L. performed stereotaxic injections. Z.L. and M.L. performed sample preparation for electrophysiology. H.H. and Z.D. performed electrophysiology experiments. Z.L. and H.H. performed analysis for electrophysiology data. Y.L., M.L. and Z.W. performed statistical analysis for behavioural assays. M.L. and X.C. performed mice genotyping. Y.L., B.M. and M.C. wrote the paper. Z.L. and M.L. reviewed the text and contributed to its revision. All authors read and approved the final manuscript. The co–first author order reflects a mutual decision.

Funding support

This research was supported in part by grant from Ministry of Education Academic Research Fund (AcRF) Singapore Tier 2 (MOE-T2EP30122-0009) and Tier 1 (FY2024-MOET1-0001).

Acknowledgements

We thank Prof Zhang Suchun (Duke-NUS) and Asst Prof Jun Nishiyama (Duke-NUS) for providing some reagents for the experiments. We thank Prof Pietro De Camili (Yale University), Prof Shirish Shenolikar (Duke University) and Prof Wang Hongyan (Duke-NUS) for reading the manuscript and providing comments. We thank Dr Sarah Luo Xinwei (IMCB-A*STAR) and Prof Enrico Petretto (Duke-NUS) for kindly providing TH-IRES-Cre mouse line and Ai9 mouse line, respectively. We also thank Prof Pietro De Camili for gifting SJ1-KI^{RQ} mouse line. We thank Asst Prof Wong Peiyan (Duke-NUS) from animal behaviour core for training. We thank Electron Microscopy Unit (NUS) for EM preparation and imaging. Some illustrations were created using BioRender. Select portions of this manuscript were edited for clarity and grammar using the ChatGPT language model (OpenAI). Scientific content and interpretations were solely formulated by the authors.

Supplemental information

Document S1. Figures S1–S12 and Table S1-S2

References

1. Bandres-Ciga S, Diez-Fairen M, Kim JJ, and Singleton AB. Genetics of Parkinson's disease: An introspection of its journey towards precision medicine. *Neurobiol Dis.* 2020;137:104782.
2. Ng XY, and Cao M. Dysfunction of synaptic endocytic trafficking in Parkinson's disease. *Neural Regen Res.* 2024;19(12):2649-60.
3. Saheki Y, and De Camilli P. Synaptic vesicle endocytosis. *Cold Spring Harbor perspectives in biology.* 2012;4(9):a005645.
4. Milosevic I, Giovedi S, Lou X, Raimondi A, Collesi C, Shen H, et al. Recruitment of Endophilin to Clathrin-Coated Pit Necks Is Required for Efficient Vesicle Uncoating after Fission. *Neuron.* 2011;72(4):587-601.
5. Verstreken P, Koh T-W, Schulze KL, Zhai RG, Hiesinger PR, Zhou Y, et al. Synaptojanin Is Recruited by Endophilin to Promote Synaptic Vesicle Uncoating. *Neuron.* 2003;40(4):733-48.
6. Schuske KR, Richmond JE, Matthies DS, Davis WS, Runz S, Rube DA, et al. Endophilin Is Required for Synaptic Vesicle Endocytosis by Localizing Synaptojanin. *Neuron.* 2003;40(4):749-62.
7. Hayashi M, Raimondi A, O'Toole E, Paradise S, Collesi C, Cremona O, et al. Cell- and stimulus-dependent heterogeneity of synaptic vesicle endocytic recycling mechanisms revealed by studies of dynamin 1-null neurons. *Proc Natl Acad Sci U S A.* 2008;105(6):2175-80.
8. Krebs CE, Karkheiran S, Powell JC, Cao M, Makarov V, Darvish H, et al. The Sac1 domain of SYNJ1 identified mutated in a family with early-onset progressive Parkinsonism with generalized seizures. *Hum Mutat.* 2013;34(9):1200-7.
9. Quadri M, Fang M, Picillo M, Olgiati S, Breedveld GJ, Graafland J, et al. Mutation in the SYNJ1 gene associated with autosomal recessive, early-onset Parkinsonism. *Hum Mutat.* 2013;34(9):1208-15.
10. Lesage S, Mangone G, Tesson C, Bertrand H, Benmahdjoub M, Kesraoui S, et al. Clinical Variability of SYNJ1-Associated Early-Onset Parkinsonism. *Front Neurol.* 2021;12:648457.
11. Dyment DA, Smith AC, Humphreys P, Schwartzentruber J, Beaulieu CL, Consortium FC, et al. Homozygous nonsense mutation in SYNJ1 associated with intractable epilepsy and tau pathology. *Neurobiology of aging.* 2015;36(2):1222 e1-5.
12. Hardies K, Cai Y, Jardel C, Jansen AC, Cao M, May P, et al. Loss of SYNJ1 dual phosphatase activity leads to early onset refractory seizures and progressive neurological decline. *Brain.* 2016;139(9):2420-30.

13. Rauschendorf MA, Jost M, Stock F, Zimmer A, Rosler B, Rijntjes M, et al. Novel compound heterozygous synaptojanin-1 mutation causes l-dopa-responsive dystonia-parkinsonism syndrome. *Mov Disord.* 2017;32(3):478-80.
14. Senkevich K, Parlar SC, Chantereault C, Yu E, Ahmad J, Ruskey JA, et al. Are rare heterozygous SYNJ1 variants associated with Parkinson's disease? *NPJ Parkinsons Dis.* 2024;10(1):201.
15. Farrow SL, Schierding W, Gokuladhas S, Golovina E, Fadason T, Cooper AA, et al. Establishing gene regulatory networks from Parkinson's disease risk loci. *Brain.* 2022;145(7):2422-35.
16. Gao X, Huang Z, Feng C, Guan C, Li R, Xie H, et al. Multimodal analysis of gene expression from postmortem brains and blood identifies synaptic vesicle trafficking genes to be associated with Parkinson's disease. *Brief Bioinform.* 2020.
17. Cremona O, Di Paolo G, Wenk MR, Luthi A, Kim WT, Takei K, et al. Essential role of phosphoinositide metabolism in synaptic vesicle recycling. *Cell.* 1999;99(2):179-88.
18. Pan PY, Sheehan P, Wang Q, Zhu X, Zhang Y, Choi I, et al. Synj1 haploinsufficiency causes dopamine neuron vulnerability and alpha-synuclein accumulation in mice. *Hum Mol Genet.* 2020;29(14):2300-12.
19. Zhu X, Prakash SS, McAuliffe G, and Pan P-Y. Synaptojanin1 Modifies Endolysosomal Parameters in Cultured Ventral Midbrain Neurons. *eneuro.* 2023;10(5).
20. Pan P-Y, Zhu J, Rizvi A, Zhu X, Tanaka H, and Dreyfus CF. Synaptojanin1 deficiency upregulates basal autophagosome formation in astrocytes. *Journal of Biological Chemistry.* 2021;297(1).
21. Cao M, Wu Y, Ashrafi G, McCartney AJ, Wheeler H, Bushong EA, et al. Parkinson Sac Domain Mutation in Synaptojanin 1 Impairs Clathrin Uncoating at Synapses and Triggers Dystrophic Changes in Dopaminergic Axons. *Neuron.* 2017;93(4):882-96 e5.
22. Ng XY, Wu Y, Lin Y, Yaqoob SM, Greene LE, De Camilli P, et al. Mutations in Parkinsonism-linked endocytic proteins synaptojanin1 and auxilin have synergistic effects on dopaminergic axonal pathology. *npj Parkinson's Disease.* 2023;9(1):26.
23. Nalls MA, Pankratz N, Lill CM, Do CB, Hernandez DG, Saad M, et al. Large-scale meta-analysis of genome-wide association data identifies six new risk loci for Parkinson's disease. *Nature Genetics.* 2014;46(9):989-93.
24. Cao M, Park D, Wu Y, and De Camilli P. Absence of Sac2/INPP5F enhances the phenotype of a Parkinson's disease mutation of synaptojanin 1. *Proc Natl Acad Sci U S A.* 2020;117(22):12428-34.

25. Pan PY, Li X, Wang J, Powell J, Wang Q, Zhang Y, et al. Parkinson's Disease-Associated LRRK2 Hyperactive Kinase Mutant Disrupts Synaptic Vesicle Trafficking in Ventral Midbrain Neurons. *J Neurosci.* 2017;37(47):11366-76.
26. Lammel S, Hetzel A, Häckel O, Jones I, Liss B, and Roeper J. Unique Properties of Mesoprefrontal Neurons within a Dual Mesocorticolimbic Dopamine System. *Neuron.* 2008;57(5):760-73.
27. Saenz J, Khezerlou E, Aggarwal M, Shaikh A, Ganti N, Herborg F, et al. Parkinson's disease gene, Synaptojanin1, dysregulates the surface maintenance of the dopamine transporter. *npj Parkinson's Disease.* 2024;10(1):148.
28. Tashiro Y, Sugimoto T, Hattori T, Uemura Y, Nagatsu I, Kikuchi H, et al. Tyrosine hydroxylase-like immunoreactive neurons in the striatum of the rat. *Neuroscience Letters.* 1989;97(1):6-10.
29. Nakahara T, Yamamoto T, Endo K, and Kayama H. Neuronal ectopic expression of tyrosine hydroxylase in the mouse striatum by combined administration of 1-methyl-4-phenyl-1,2,3,6-tetrahydropyridine and 3-nitropropionic acid. *Neuroscience.* 2001;108(4):601-10.
30. Ibáñez-Sandoval O, Tecuapetla F, Unal B, Shah F, Koós T, and Tepper JM. Electrophysiological and Morphological Characteristics and Synaptic Connectivity of Tyrosine Hydroxylase-Expressing Neurons in Adult Mouse Striatum. *The Journal of Neuroscience.* 2010;30(20):6999-7016.
31. Dubach M, Schmidt R, Kunkel D, Bowden DM, Martin R, and German DC. Primate neostriatal neurons containing tyrosine hydroxylase: Immunohistochemical evidence. *Neuroscience Letters.* 1987;75(2):205-10.
32. Betarbet R, Turner R, Chockkan V, DeLong MR, Allers KA, Walters J, et al. Dopaminergic neurons intrinsic to the primate striatum. *J Neurosci.* 1997;17(17):6761-8.
33. Porritt MJ, Batchelor PE, Hughes AJ, Kalnins R, Donnan GA, and Howells DW. New dopaminergic neurons in Parkinson's disease striatum. *Lancet.* 2000;356(9223):44-5.
34. Cossette M, Lecomte F, and Parent A. Morphology and distribution of dopaminergic neurons intrinsic to the human striatum. *J Chem Neuroanat.* 2005;29(1):1-11.
35. Huot P, Levesque M, and Parent A. The fate of striatal dopaminergic neurons in Parkinson's disease and Huntington's chorea. *Brain.* 2006;130(1):222-32.
36. Xenias HS, Ibáñez-Sandoval O, Koós T, and Tepper JM. Are Striatal Tyrosine Hydroxylase Interneurons Dopaminergic? *The Journal of Neuroscience.* 2015;35(16):6584-99.

37. Tepper JM, Koós T, Ibanez-Sandoval O, Tecuapetla F, Faust TW, and Assous M. Heterogeneity and Diversity of Striatal GABAergic Interneurons: Update 2018. *Frontiers in Neuroanatomy.* 2018;12:91.

38. Darmopil S, Muñetón‐Gómez VC, De Ceballos ML, Bernson M, and Moratalla R. Tyrosine hydroxylase cells appearing in the mouse striatum after dopamine denervation are likely to be projection neurones regulated by l‐DOPA. *European Journal of Neuroscience.* 2008;27(3):580-92.

39. Masuda M, Miura M, Inoue R, Imanishi M, Saino‐Saito S, Takada M, et al. Postnatal development of tyrosine hydroxylase mRNA‐expressing neurons in mouse neostriatum. *European Journal of Neuroscience.* 2011;34(9):1355-67.

40. Mao M, Nair A, and Augustine GJ. A Novel Type of Neuron Within the Dorsal Striatum. *Frontiers in Neural Circuits.* 2019;13:32.

41. Liu G, Yu J, Ding J, Xie C, Sun L, Rudenko I, et al. Aldehyde dehydrogenase 1 defines and protects a nigrostriatal dopaminergic neuron subpopulation. *The Journal of Clinical Investigation.* 2014;124(7):3032-46.

42. Hadjas LC, Kollman GJ, Linderhof L, Xia M, Mansur S, Saint-Pierre M, et al. Parkinson's Disease-vulnerable and -resilient dopamine neurons display opposite responses to excitatory input. *bioRxiv.* 2025:2025.06.03.657460.

43. Mantas I, Contestabile A, Skara V, Loiseau C, Santos IA, Cramb KML, et al. Anxa1+ dopamine neuron vulnerability defines prodromal Parkinson's disease bradykinesia and procedural motor learning impairment. *bioRxiv.* 2025:2024.12.22.629963.

44. Fushiki A, Ng D, Lewis ZR, Yadav A, Saraiva T, Hammond LA, et al. A Vulnerable Subtype of Dopaminergic Neurons Drives Early Motor Deficits in Parkinson's Disease. *bioRxiv.* 2026:2024.12.20.629776.

45. Azcorra M, Gaertner Z, Davidson C, He Q, Kim H, Nagappan S, et al. Unique functional responses differentially map onto genetic subtypes of dopamine neurons. *Nature Neuroscience.* 2023;26(10):1762-74.

46. Anderegg A, Poulin J-F, and Awatramani R. Molecular heterogeneity of midbrain dopaminergic neurons – Moving toward single cell resolution. *FEBS Letters.* 2015;589(24PartA):3714-26.

47. Ibáñez-Sandoval O, Xenias HS, Tepper JM, and Koós T. Dopaminergic and cholinergic modulation of striatal tyrosine hydroxylase interneurons. *Neuropharmacology.* 2015;95:468-76.

48. Ünal B, Shah F, Kothari J, and Tepper JM. Anatomical and electrophysiological changes in striatal TH interneurons after loss of the nigrostriatal dopaminergic pathway. *Brain Structure and Function.* 2015;220(1):331-49.

49. Assous M, Faust TW, Assini R, Shah F, Sidibe Y, and Tepper JM. Identification and Characterization of a Novel Spontaneously Active Bursty GABAergic Interneuron in the Mouse Striatum. *The Journal of Neuroscience.* 2018;38(25):5688-99.
50. Palfi S, Leventhal L, Chu Y, Ma SY, Emborg M, Bakay R, et al. Lentivirally Delivered Glial Cell Line-Derived Neurotrophic Factor Increases the Number of Striatal Dopaminergic Neurons in Primate Models of Nigrostriatal Degeneration. *The Journal of Neuroscience.* 2002;22(12):4942.
51. Tande D, Hoglinger G, Debeir T, Freundlieb N, Hirsch EC, and Francois C. New striatal dopamine neurons in MPTP-treated macaques result from a phenotypic shift and not neurogenesis. *Brain.* 2006;129(Pt 5):1194-200.
52. Troshev D, Bannikova A, Blokhin V, Pavlova E, Kolacheva A, and Ugrumov M. Compensatory Processes in Striatal Neurons Expressing the Tyrosine Hydroxylase Gene in Transgenic Mice in a Model of Parkinson's Disease. *International Journal of Molecular Sciences.* 2023;24(22):16245.
53. Erben L, Welday JP, Murphy R, and Buonanno A. *International Journal of Molecular Sciences*. 2022.
54. Rezai Amin S, Gruszczynski C, Guiard BP, Callebert J, Launay J-M, Louis F, et al. Viral vector-mediated Cre recombinase expression in substantia nigra induces lesions of the nigrostriatal pathway associated with perturbations of dopamine-related behaviors and hallmarks of programmed cell death. *Journal of Neurochemistry.* 2019;150(3):330-40.
55. Özçete ÖD, Banerjee A, and Kaeser PS. Mechanisms of neuromodulatory volume transmission. *Molecular Psychiatry.* 2024;29(11):3680-93.
56. Chanaday NL, Cousin MA, Milosevic I, Watanabe S, and Morgan JR. The Synaptic Vesicle Cycle Revisited: New Insights into the Modes and Mechanisms. *The Journal of Neuroscience.* 2019;39(42):8209.
57. Mejaes JI, Saenz J, O'Brien C, Pizzano CM, Pan PY, and Barker DJ. Haploinsufficiency of the Parkinson's disease gene synaptojanin1 is associated with abnormal responses to psychomotor stimulants and mesolimbic dopamine signaling. *Front Behav Neurosci.* 2024;18:1359225.
58. Delignat-Lavaud B, Kano J, Ducrot C, Masse I, Mukherjee S, Giguere N, et al. Synaptotagmin-1-dependent phasic axonal dopamine release is dispensable for basic motor behaviors in mice. *Nat Commun.* 2023;14(1):4120.
59. Cai X, Liu C, Tsutsui-Kimura I, Lee J-H, Guo C, Banerjee A, et al. Dopamine dynamics are dispensable for movement but promote reward responses. *Nature.* 2024;635(8038):406-14.

60. Troshev D, Bannikova A, Blokhin V, Kolacheva A, Pronina T, and Ugrumov M. Striatal Neurons Partially Expressing a Dopaminergic Phenotype: Functional Significance and Regulation. *International Journal of Molecular Sciences.* 2022;23(19):11054.

61. Rice ME, Patel JC, and Cragg SJ. Dopamine release in the basal ganglia. *Neuroscience.* 2011;198:112-37.

62. Busceti CL, Bucci D, Molinaro G, Di Pietro P, Zangrandi L, Gradini R, et al. Lack or Inhibition of Dopaminergic Stimulation Induces a Development Increase of Striatal Tyrosine Hydroxylase-Positive Interneurons. *PloS one.* 2012;7(9):e44025.

Figure Legends

Figure 1 SJ1 conditional KO (SJ1 cKO^{DAT}) in DA neurons exhibit dystrophic DA axon terminals in the striatum

(A) Generation of SJ1 cKO^{DAT} mice by crossing SJ1 flx/flx mice with DAT-IRES-Cre line to create DA-specific SJ1 conditional KO mice (DAT-Cre;SJ1 flx/flx), hereafter referred to as SJ1 cKO^{DAT}. Appropriate littermate control (SJ1 flx/flx or DAT-Cre;SJ1+/flx) were used in all experiments.

(B) Double staining of TH and SJ1 to show SJ1 specifically KO in midbrain DA neurons. Green arrows: TH-positive DA neurons; White arrows: TH-negative midbrain neurons. SJ1 expression in hippocampus shows that other regions were not affected. Scale bar: 20 μm.

(C) Immunofluorescence analysis reveals significant reduction of SJ1 intensity in both SNc and VTA of SJ1 cKO^{DAT} compared to controls, confirming specific knockout in DA neurons. Mean fluorescence intensity of SJ1 was quantified and expressed as a percentage of control values. Data are represented as mean ± SEM. n=3 mice per genotype.

(D) DAT staining of 2 months old Ctrl and SJ1 cKO^{DAT} shows clustering phenotype in dorsal (DS) and ventral striatum (VS). Scale bar: 20 μm.

(E) Quantification for DAT clusters at 2-3 months and 6-8 months of age. The average number of clusters is counted in five randomly selected, 300 × 300-μm regions of interest (ROIs). Data are represented as mean ± SEM (*$p<0.01$ and ***$p<0.001$ by one-way ANOVA with post-hoc Tukey's test). n=3 mice per genotype.

(F) Double staining of DAT with TH, AADC, vMAT2 and SV2C showed co-clustering in the dorsal striatum (DS) of SJ1 cKO^{DAT} mice. Scale bar: 20 μm.

(G) Pearson's correlation coefficient for striatum double staining shown in (F) reveals strong linear relationship between DAT with TH, AADC, vMAT2 and SV2C. Data are represented as mean ± SEM.

(H) Representative EM micrographs of nerve terminals from the ventral striatum (VS) of SJ1 cKO^{DAT}. Red arrows: "Whirl"-like multilayered membranes; Synaptic vesicles (SVs), endosomes (endo), autophagosome (AP) and mitochondria (mt) were also labelled in the images. Scale bar: 500 nm.

Figure 2 Dysregulated DA system and impaired DA release in SJ1 cKO^{DAT} striatum

(A), (B) Representative western blot and analysis for DA markers, endocytic and general synaptic markers from 2-3 months old Ctrl and SJ1 cKO^{DAT} half brain striatal homogenates. DAT and vMAT2 in SJ1 cKO^{DAT} exhibited significant reduction after normalization. Data are represented as mean ± SEM (*p<0.05 and **p<0.01 with Welch's unpaired t-test). n=3-5 mice per genotype.

(C), (D) HPLC analysis of total DA content in the striatum of SJ1 cKO^{DAT} mice showed an average of 50% reduction in striatal DA level, enhanced HVA level and non-significant change in DOPAC level for 2-3 months old (C) and 6-8 months old (D). Data are represented as mean ± SEM (*p<0.05 and **p<0.01 with Welch's unpaired t-test). n number used for each genotype=5 for 2-3M; n=6 for 6-8M.

(E) Illustration of KCl-evoked DA release in DA terminals.

(F) Illustration of AMPH-induced DA efflux in DA terminals.

(G) Quantification of normalized DA concentration from KCl-evoke DA release in SJ1 cKO^{DAT} acute striatal slices (age range 2-9M) revealed significant reduction, suggesting impaired vesicular release. Data are represented as mean ± SEM (*p<0.05 with Welch's unpaired t-test). n=5 mice per genotype.

(H) Quantification of normalized DA concentration from AMPH-induced DA efflux in SJ1 cKO^{DAT} acute striatal slices (age range 2-9M) revealed significant reduction, suggesting reduced DAT-mediated DA efflux. Data are represented as mean ± SEM (**p<0.01 with Welch's unpaired t-test). n=5 mice per genotype.

Figure 3 SJ1 cKO^{DAT} displayed altered locomotor activity but no coordination deficit

(A) Representative open-field activity traces (15 min) from Ctrl and SJ1 cKO^{DAT} mice at both time points illustrate reduced locomotor activity observed in mutants.

(B) Total distance traveled in open field test was recorded for 15 min. Significant p-value for total distance at both 2-4 and 6-8 months old SJ1 cKO^{DAT} mice indicate reduced spontaneous locomotion during baseline. Data are represented as mean ± SEM (*p<0.05 and **p<0.01 with Welch's unpaired t-test). n numbers used for each age group (2-4M: 7; 6-8M: 6).

(C), (D) Quantification of average distance traveled, expressed as percent of baseline, over the time course. Locomotor activity (% of baseline) of SJ1 cKO^{DAT} mice increased over 60 min session treated with 3mg/kg amphetamine (AMPH). Data are represented as mean ± SEM (*p<0.05 and **p<0.01 by two-way repeated measures ANOVA with post-hoc Tukey's test). n numbers used for each age group (2-4M: 7; 6-8M: 6).

(E) Representative open-field activity traces (60 min) from Ctrl and SJ1 cKO^{DAT} mice at both time points illustrate AMPH-induced heightened hyperactivity observed in mutants.

(F), (G) Average traveled distance in the open field. % of baseline across 60 min session in 2-4 (F) and 6-8 (G) months old treated with 3 mg/kg AMPH show significant increase in mutant's locomotion. Data are represented as mean ± SEM (*p<0.05, **p<0.01 by Welch's t test). n numbers used for each age group (2-4M: 7; 6-8M: 6).

(H), (I) Average total distance traveled over the time course (H) and average distance traveled in open field (I), both expressed as percent of baseline, showing significantly elevated locomotion in SJ1 cKO^{DAT} mice (age range 4-10M) in response to D1R agonist, SKF81297 at 2.5mg/kg. Data are represented as mean ± SEM (*p<0.05 and **p<0.01 by two-way repeated measures ANOVA with post-hoc Tukey's test). n=6 per genotype.

(J), (K) Average total distance traveled over the time course (H) and average distance traveled in open field (I), both expressed as percent of baseline, showing comparable reduced locomotion in Ctrl and SJ1 cKO^{DAT} mice (age range 6-8M) in response to D2R agonist, quinpirole at 0.2mg/kg. Data are represented as mean ± SEM. n=6 per genotype.

(L) Accelerated rotarod performance of two age groups. Latency to fall did not differ significantly between Ctrl and SJ1 cKO^{DAT} mice. Data are represented as mean ± SEM. n numbers used for Ctrl and SJ1 cKO^{DAT} mice (2–3M: 13 and 15; 6–8 M: 9 and 10).

(M) Number of missteps during the balance beam test did not differ significantly between Ctrl and SJ1 cKO^{DAT} mice. Data are represented as mean ± SEM. n numbers used for Ctrl and SJ1 cKO^{DAT} mice (2–3M: 13 and 15; 6–8M: 9 and 10).

Figure 4 Robust appearance of induced TH-positive interneurons (iTHINs) with DA-like characteristics in the SJ1 cKO^{DAT} striatum

(A) TH immunostaining detected robust emergence of iTHINs observed in the striatum of 2 months old SJ1 cKO^{DAT} mice but not in Ctrl. Scale bar: 50 µm.

(B) Quantification of iTHINs in 2-3 months and 6-8 months shows significant higher number in SJ1 cKO^{DAT} striatum. Number of iTHINs were quantified on single coronal striatum section of one hemisphere. Data are represented as mean ± SEM (**p<0.01). n=3 mice per genotype.

(C) Representative image of iTHINs co-expressing TH and AADC in the striatum of 2 months old SJ1 cKO^{DAT} mice compared to Ctrl. White arrows: iTHINs. Asterisk: clusters. Scale bar: 20 µm.

(D) Double staining of vMAT2 and DAT with TH shows vMAT2 and DAT are clustered with TH at DA terminals but not expressed in iTHINs in 2 months old SJ1 cKO^{DAT} striatum. White arrows: iTHINs. Asterisk: clusters. Scale bar: 20 µm.

(E) Violin plots of enrichment ratios. Using a 1.5-fold threshold, AADC showed strong enrichment in TH-positive neurons, with enrichment ratios clearly shifted above baseline compared to vMAT2 and DAT.

(F) Simplified schematic illustration of ALDH1A1 labelling in SNc and striatum.

(G), (H) Double staining of ALDH1A1 and TH shows ALDH1A1 is detected in both dystrophic DA terminals and iTHINs in SJ1 cKO^{DAT} dorsal (G) but not ventral (H) striatum. White arrows: iTHINs. Asterisk: clusters. Scale bar: 50 µm.

(I) Simplified schematic illustration of Anxa1 labelling in SNc and striatum.

(J), (K) Double staining of Annexin A1 and TH shows Annexin A1 is detected in subpopulation of iTHINs in SJ1 cKO^{DAT} dorsal (J) but not ventral (K) striatum. White arrows: iTHINs. Scale bar: 50 µm.

Figure 5 SJ1 conditional KO using TH-IRES-Cre (SJ1 cKOTH) phenocopies SJ1 cKO^{DAT} pathological characteristics

(A) Generation of SJ1 cKOTH mice by crossing SJ1 flx/flx mice with TH-IRES-Cre line to create TH-specific SJ1 conditional KO mice (TH-Cre;SJ1 flx/flx), hereafter referred to as SJ1

cKOTH. Appropriate littermate controls (SJ1 flx/flx or TH-Cre;SJ1 +/flx) were used in all experiments.

(B) Double staining of TH and SJ1 showed specific loss of SJ1 in DA neurons. SJ1 expression in hippocampus shows that other regions were not affected. Scale bar: 20 μm.

(C) Immunofluorescence analysis reveals significant reduction of SJ1 intensity in both SNc and VTA of SJ1 cKOTH compared to controls, confirming specific knockout in DA neurons. Mean fluorescence intensity of SJ1 was quantified and expressed as a percentage of control values. Data are represented as mean ± SEM.

(D) DAT staining of 2 months old Ctrl and SJ1 cKOTH showed similar clustering phenotype in dorsal and ventral striatum. Scale bar: 20 μm.

(E) Double staining of SV2C with vMAT2, TH with DAT and AADC showed the same dystrophic DA terminal pathology positive for all the markers in SJ1 cKOTH striatum (asterisk). In addition, iTHINs (white arrows) were robustly induced, which co-expressed TH and AADC, but not DAT. Scale bar: 20 μm.

(F) Violin plots of enrichment ratios. Using a 1.5-fold threshold, AADC showed strong enrichment in TH-positive neurons, with enrichment ratios clearly shifted above baseline compared to DAT.

(G), (H) Double staining of ALDH1A1 and TH shows ALDH1A1 is detected in both dystrophic DA terminals (asterik) and iTHINs (white arrows) in SJ1 cKOTH dorsal (G) but not ventral (H) striatum. Scale bar: 50 μm.

(I) Violin plots of enrichment ratios. Using a 1.5-fold threshold, ALDH1A1 showed strong enrichment in dorsal striatum (DS) TH-positive neurons, with enrichment ratios clearly shifted above baseline compared to those in ventral striatum (VS).

Figure 6 Cre-dependent reporter lines label WT THINs and iTHINs in different patterns

(A) Simplified schematic showing the generation of Ai9-tdT labelled SJ1 cKOTH and SJ1 cKO^{DAT} mice, referred to as Ai9;SJ1 cKOTH and Ai9;SJ1 cKO^{DAT}, respectively. Ai9-tdT reporter driven by CAG promoter expresses DA-specific tdT signal after Cre-mediated recombination by either TH- or DAT-IRES-Cre line.

(B) Representative images of tdT expression shown in the midbrain TH-positive DA neurons of 2 months old Ai9;TH-Cre (Ctrl) and Ai9;SJ1 cKOTH. Scale bar: 100 µm.

(C) Representative images of tdT expression shown in the midbrain TH-positive DA neurons in the midbrain of 2 months old Ai9;DAT-Cre (Ctrl) and Ai9;SJ1cKO^{DAT}. Scale bar: 100 µm.

(D) Representative images of tdT expression and immunostaining of TH in the striatum of 2 months old Ai9;TH-Cre (Ctrl) and Ai9;SJ1 cKOTH. Blue arrows: tdT expressing THINs driven by TH-Cre recombination (negative for TH immunostaining). White arrows: iTHINs expressing tdT signal (positive for TH immunostaining). Scale bar: 50 µm.

(E) Percentage of TH-Cre driven tdT expressing neurons positive for TH immunostaining shown in (D). In average, 34.11% of total tdT expressing neurons were positive for TH immunostaining (iTHINs). The number of neurons was quantified on a single stitched coronal striatum section for both tdT expressing neurons and tdT/TH-positive neurons. Data are represented as mean ± SEM. n=3 mice per genotype.

(F) Quantification of the average long soma diameter of WT THINs and iTHINs showed no significant differences in cell size. Data are represented as mean ± SEM. n=3 mice.

(G) The average tdT fluorescence intensity of WT THINs (blue arrow) is significantly higher than iTHINs (white arrow) when compared in the striatum of Ai9;SJ1 cKOTH. Data are represented as mean ± SEM. n=4 mice. Scale bar: 10 µm.

(H) Representative images of tdT expression and immunostaining of TH and DAT in the striatum of Ai9;DAT-Cre (Ctrl) and Ai9;SJ1cKO^{DAT}. tdT expressing striatal neurons were positive for TH but not DAT immunostaining (white arrows). Scale bar: 50 µm.

(I) Percentage of tdT expressing neurons positive for TH immunostaining in DAT-Cre dependant background shown in (H). Majority of tdT expressing neurons were iTHINs. The number of neurons was quantified on a single stitched coronal striatum section for both tdT expressing neurons and tdT/TH-positive neurons. Data are represented as mean ± SEM. n=3 mice per genotype.

Figure 7 iTHINs form a distinct electrophysiological subcluster with reduced intrinsic excitability compared to WT THINs

(A) Representative images of Ai9;TH-Cre and Ai9;SJ1cKO^{DAT} showing WT THINs (blue arrow, tdT-TH positive and TH-negative) and iTHINs (white arrow, tdT-DAT positive and TH positive). Scale bar: 50 µm.

(B) Representative images of a patch-clamped tdT-positive iTHIN in the dorsal striatum. Upper: differential interference contrast (DIC) image shows the patched neuron. Lower: epifluorescence image shows tdT (RFP filter) expression in the same cell. Scale bar: 20 µm.

(C) A representative three-dimensional scatter plot showing clustering of WT THINs (left) into three electrophysiological subtypes. Overlay of iTHINs (right) recorded from Ai9;SJ1 cKO^{DAT} mice onto the same three-dimensional feature space reveals that iTHINs occupy a distinct region that is distinct from three other WT THINs clusters.

(D) Radar plot summarizing normalized population mean values (0–1 scale) of 14 electrophysiological parameters for the three WT THIN clusters and iTHINs, revealing distinct profiles across the four cell groups.

(E) Representative traces of the first action potential elicited in WT THIN clusters and iTHINs. iTHINs show action potential waveform properties that differ from WT cluster 1 and cluster 3, while closely resemble those of WT cluster 2.

(F) Representative evoked firing traces of the three WT THIN clusters and iTHINs in response to current injection. Notably, WT THIN cluster 2 exhibits a prolonged depolarizing plateau potential (red box), which is absent in iTHINs.

(G) Bar charts comparing four representative electrophysiological parameters among WT THIN clusters and iTHINs, including plateau potential duration, input resistance, resting membrane potential (RMP), and spontaneous activity. Consistent with reduced intrinsic excitability inferred from passive membrane properties, iTHINs exhibited altered membrane parameters compared to WT THINs. Data are presented as mean ± SEM. Statistical significance was assessed using the Kruskal–Wallis test followed by Dunn's multiple comparison test. (**$p < 0.01$, ***$p < 0.001$, ****$p < 0.001$.)

Figure 8 THINs appearing in 6-OHDA and Casp3 lesion mice are distinct from iTHINs observed in SJ1 cKO mice

(A) Schematic showing the midbrain of 2-3 months old B6 mice unilaterally injected with 6-OHDA and collected 2 weeks post injection for IHC.

(B) Schematic showing the midbrain of 2-3 months old DAT-Cre mice unilaterally injected with pAAV-flex-taCasp3-TEVp (Cre-dependent) and collected 2 weeks post injection for IHC.

(C) Representative coronal section shows the extent of 6-OHDA lesion in the striatum and midbrain DA neurons of B6 mice. Scale bar: 500 µm.

(D) Representative coronal section shows the extent of Casp3-mediated lesion in the striatum and midbrain DA neurons of DAT-Cre mice. Scale bar: 500 µm.

(E) Representative images of TH-positive neurons (white arrows) observed in the striatum of SJ1 cKO^{DAT} and lesioned hemisphere of 6-OHDA and Casp3 injected mice. Exposure time and threshold were set the same for anti-TH imaging in all three conditions. Scale bar: 20 µm.

(F) The expression level of TH protein observed in 6-OHDA and Casp3 lesioned models is significantly lower than iTHINs observed in SJ1 cKO^{DAT} striatum. Data are represented as mean ± SEM (****$p<0.0001$ by one-way ANOVA with post hoc Tukey's test). n=3 mice per genotype.

(G) Unlike iTHINs in SJ1 cKO^{DAT} mice, AADC is undetectable in either 6-OHDA or Casp3 lesioned striatum. Scale bar: 20 µm.

(H) Unlike iTHINs in SJ1 cKO^{DAT} mice, ALDH1A1 is undetectable in either 6-OHDA or Casp3 lesioned striatum. Scale bar: 20 µm.

Figure 9 Acute SJ1 KO in DA neurons of adult and aged mice triggers similar DA terminal pathology but fewer iTHINs

(A) Schematic showing unilateral stereotaxic injection of AAV9-TH-Cre virus into the ventral midbrain of 2 months (adult) or 12 months (aged) SJ1 flx/flx mice to obtain SJ1 acute KO in DA neurons. Animal brains were collected 3-4 months post injection for IHC.

(B) TH and SJ1 immunostaining of the adult and aged SJ1 acute KO mice showed SJ1 specific KO in the injected midbrains. Scale bar: 100 µm.

(C) Immunofluorescence analysis of SJ1 intensity in DA neurons of injected hemisphere shows reduction (not significant) compared to contralateral hemisphere. Mean fluorescence intensity of SJ1 was quantified and expressed as a percentage of control values. Data are represented as mean ± SEM. n=2 mice per genotype.

(D) DAT immunostaining of the adult and aged SJ1 acute KO mice shows similar clustering phenotype in dorsal (DS) and ventral striatum (VS) as observed in SJ1 cKO^{DAT} mice. Scale bar: 20 µm.

(E) No significant difference of the number of DAT clusters between SJ1 cKO^{DAT}, adult and aged SJ1 acute KO. The average number of clusters is counted in five randomly selected, 300 × 300-µm regions of interest (ROIs). Data are represented as mean ± SEM. n = 3-4 mice per genotype.

(F) Representative images of striatum show comparable TH/DAT-positive clusters but much lesser iTHINs in the injected hemisphere of adult and aged SJ1 acute KO mice when compared to the striatum of SJ1 cKO^{DAT} mice. White arrows: iTHINs. Scale bar: 50 µm.

(G) Number of iTHINs in the adult and aged SJ1 acute KO is significantly lower than SJ1 cKO^{DAT} mice. Number of iTHINs was quantified in stitched coronal section of the injected striatum. Data are represented as mean ± SEM (**$p<0.01$). n=3-4 mice per genotype.

Supplementary Figure Legends

Supplementary Figure 1 Further characterization of DA system in SJ1 cKO^{DAT} mice

(A) Stereological analysis of TH-positive DA cell bodies in the SNc and VTA region of Ctrl and SJ1 cKO^{DAT} mice at 2-3 months and 6-8 months age group. There is no significant loss of DA neurons in both ages. The estimated cell numbers in one hemisphere are shown. Data are represented as mean ± SEM. n=3 mice per genotype. Scale bar: 200 µm.

(B) Representative images of DAT immunostaining in the striatum of SJ1 cKO^{DAT} at 3 weeks, 2 months, 6 months and 12 months age group. Scale bar: 50 µm.

(C), (D) Tiling of a single coronal striatum section labelled for DAT in 2 months SJ1 cKO^{DAT} (C) and SJ1-KI^{RQ} mice (D). Unlike SJ1-KI^{RQ} that showed clusters in dorsal striatum only, DAT clusters were observed in most of the striatum region of SJ1 cKO^{DAT} mice, including dorsal striatum (DS), ventral striatum (VS) and olfactory tubercle (OT). Scale bar: 500 µm. Inset scale bar: 50 µm.

(E) TH and DAT immunostaining in nucleus accumbens (NAc) core showing TH and DAT positive clusters in the striatum of SJ1 cKO^{DAT} mice Scale bar: 50 µm.

(F) TH and DAT immunostaining in nucleus accumbens (NAc) medial shell reveals lack of DAT signal and intact TH fibers in both control and SJ1 cKO^{DAT} mice Scale bar: 50 µm.

(G), (H) TH and DAT immunostaining of the prefrontal cortex (PFC) region (G) and basolateral amygdala (BLA) region (H), both receiving DA projections from the VTA shows intact TH fibers and lack of DAT expression. No obvious differences in TH-positive fibers were observed between control and mutant mice. Scale bar: 50 µm.

Supplementary Figure 2 Other markers examined in the SJ1 cKO^{DAT} striatum

(A) Immunostaining of vMAT2 with SV2C showed colocalization for clusters in the striatum of 2 months SJ1 cKO^{DAT} mice. Scale bar: 20 µm.

(B) Immunostaining of DAT with Syt1 showed partial colocalization with DAT-positive clusters in the striatum of 2 months SJ1 cKO^{DAT} mice. Scale bar: 20 µm.

(C), (D) Immunostaining of DAT with postsynaptic markers, D2R (C) and D1R (D), showed no colocalization with DAT-positive clusters in the striatum of 2 months SJ1 cKO^{DAT} mice, suggesting there is no effect on postsynaptic neurons. Scale bar: 20 μm.

(E) Immunostaining of DAT with Darpp32 showed no colocalization with DAT-positive clusters in the striatum of 2 months SJ1 cKO^{DAT} mice. Scale bar: 20 μm.

(F) Quantification of colocalization using Pearson's correlation coefficient reflects the visual relationships shown in the striatum of SJ1 cKO^{DAT} mice (A–E). Higher r value for SV2C/vMAT2 indicate strong linear correlation, while other markers with lower r values show moderate to weak relationship. Data are represented as mean ± SEM. Data was computed using 4–6 randomly selected ROIs in the striatum.

Supplementary Figure 3 Neuronal and inflammation markers examined in the SJ1 cKO^{DAT} striatum

(A), (B) Immunostaining of DAT with GFAP (A) and Iba1 (B) showed similar glia cell pattern in both Ctrl and SJ1 cKO^{DAT} mice at 2 months old, suggesting there is no gliosis and inflammation in the striatum. Scale bar: 20 μm.

(C) GFAP and Iba1 immunoreactive area fraction in the striatum of Ctrl and SJ1 cKO^{DAT} mice at 2 months old reveals no significant differences. Data are represented as mean ± SEM. n=3 per genotype.

(D) Immunostaining of alpha-Synuclein showed partial colocalization with DAT-positive clusters in the striatum of 2 months SJ1 cKO^{DAT} mice. Scale bar: 20 μm.

(E), (F) Immunostaining of pSer129-alpha-Synuclein with DAT (E) and TH (F) showed no detection of misfolded alpha-Synuclein in DAT-positive clusters and DA neurons, respectively, at 2 months old. Scale bar: 20 μm.

(G) Pearson's correlation coefficient reflects the visual relationships shown in (D) and (E), showing mild and weak relationship, respectively. Data are represented as mean ± SEM. Data was computed using 4–5 randomly selected ROIs in the striatum.

Supplementary Figure 4 Endocytic markers examined in the SJ1 cKO^{DAT} striatum

(A)-(D) Double staining of DAT with SJ1 (A), clathrin-light chain (CLC) (B), amphiphysin 1 (C) and endophilin 1 (D) showed no colocalization of these clathrin-related endocytic proteins with DAT-positive clusters in the striatum of 2 months old SJ1 cKO^{DAT} mice. Scale bar: 20 µm.

(E) Pearson's correlation coefficient reflects the visual relationships shown in (A)-(D), reflecting low colocalization between the endocytic proteins and the clusters. Data are represented as mean ± SEM. Data was computed using 3 randomly selected ROIs in the striatum.

Supplementary Figure 5 More EM images of whirl-like membrane accumulation at DA terminals in SJ1 cKO^{DAT} striatum

(A), (B) More representative EM images to show the abnormal lipid membrane accumulation which is correlated with DAT/TH-positive protein clusters in 2 months old SJ1 cKO^{DAT} ventral striatum. Abnormal whirl-like multilayered membrane (red arrows) surrounding the synaptic vesicles (SVs) and endosomes (endo). Mitochondria (mt) also labelled in the terminals. Scale bar: 200 nm and 500nm.

Supplementary Figure 6 Distribution of iTHINs in whole striatum of SJ1 cKO^{DAT}

(A) Tiling of a single coronal striatum section with TH immunostaining in 2 months old SJ1 cKO^{DAT} mice. Insets: TH-positive clusters and iTHINs were both observed throughout the striatum, including dorsal striatum (DS), ventral striatum (VS) and olfactory tubercle (OT). Scale bar: 500 µm.

(B) Representative images of TH immunostaining in the striatum of SJ1 cKO^{DAT} at 3 weeks, 2 months, 6 months and 12 months age group. TH-positive iTHINs (white arrows) and clusters (asterisk) were labelled. Scale bar: 50 µm.

(C) Quantification of iTHINs in the striatum of SJ1 cKO^{DAT} mice from 3 weeks to 12 months old. Number of iTHINs were quantified on single coronal striatum sections of one hemisphere. Data are represented as mean ± SEM. n= 1-3 mice.

Supplementary Figure 7 iTHINs are a distinct group of striatal interneurons

(A)-(C) Immunostaining of TH with NPY (A), PV (B) and ChAT (C) in SJ1 cKO^{DAT} striatum showed that iTHINs is a distinct group of neurons from other striatal interneurons. Scale bar: 20 µm.

(D), (E) Very few iTHINs in the striatum of SJ1 cKO^{DAT} occasionally co-express Calretinin (D) and Darpp32 (E), suggesting heterogeneity within iTHINs subpopulation. Scale bar: 20 µm.

Supplementary Figure 8 A subpopulation of iTHINs in SJ1 cKO^{DAT} dorsal striatum expresses ALDH1A1 and Anxa1

(A) Immunostaining of TH and ALDH1A1 in the midbrain of 2 months old mice shows enriched ALDH1A1 in the ventral tier of SNc DA neurons in both genotypes. Scale bar: 200 µm.

(B) Tiling of a single coronal striatum section immunostained for TH and ALDH1A1 of 2 months old Ctrl and SJ1 cKO^{DAT} mice. TH/ALDH1A1-positive iTHINs were mainly distributed in dorsal striatum (DS). Scale bar: 500 µm

(C) Immunostaining of TH and Anxa1 in the midbrain of 2 months old mice shows Anxa1 is enriched in the ventral tier of SNc DA neurons in both genotypes. Scale bar: 200 µm.

(D) Immunostaining shows Anxa1-positive DA neurons within a subpopulation of ALDH1A1-positive DA neurons in the midbrain of 2 months old mice. Scale bar: 200 µm.

(E) A subset of ALDH1A1-positive striatal interneurons are positive for Anxa1 in the dorsal-lateral striatum of SJ1 cKO^{DAT} mice (white arrows). Scale bar: 50 µm.

(F) Simplified illustrations of Calbindin distribution in the midbrain and striatum.

(G) Immunostaining of TH and Calbindin in the midbrain of 2 months old mice show some VTA DA neurons expressing Calbindin. Scale bar: 20 µm.

(H) Immunostaining of TH and Calbindin shows that Calbindin was not detected in iTHINs of the ventral striatum of 2 months old SJ1 cKO^{DAT}. Scale bar: 50 µm.

Supplementary Figure 9 Electrophysiological properties of WT THINs and iTHINs

(A) Bar charts showing the proportion of WT THINs and iTHINs within each of the four clusters identified by PCA-based clustering of the combined dataset. Data from WT THINs and iTHINs were pooled prior to dimensionality reduction and clustering.

(B) Bar charts comparing ten representative electrophysiological parameters among 3 WT THIN clusters and iTHINs, including action potential (AP) width at 50% relative to baseline and threshold, AP amplitude relative to baseline and threshold, AP threshold, maximal firing frequency, after-hyperpolarization (AHP) amplitude, hyperpolarization-activated current (Ih ratio), membrane capacitance and low-threshold spike (LTS). Data are presented as mean ± SEM. Statistical significance was assessed using the Kruskal–Wallis test followed by Dunn's multiple comparison test (**$p < 0.01$, ***$p < 0.001$, ****$p < 0.001$).

Supplementary Figure 10 Electrophysiological properties of SNc and VTA DA neurons in control and SJ1 cKO^{DAT} mice

(A) Representative images of a patch-clamped tdT-positive DA neuron in the SNc. Upper: differential interference contrast (DIC) image showing the patched neuron. Lower: epifluorescence image showing tdTomato (RFP) expression in the same cell. Scale bar: 20 µm.

(B) Spontaneous firing of Ctrl and SJ1 cKO^{DAT} SNc DA neurons recorded in cell-attached (on-cell) configuration.

(C) Intrinsic firing of Ctrl and SJ1 cKO^{DAT} SNc DA neurons recorded in whole-cell current-clamp mode (I = 0 pA).

(D) Representative evoked firing traces of Ctrl and SJ1 cKO^{DAT} SNc DA neurons.

(E) Representative traces of the first action potential elicited in Ctrl and SJ1 cKO^{DAT} SNc DA neurons.

(F) Bar charts comparing Ctrl and SJ1 cKO^{DAT} SNc DA neurons. Compared to Ctrl, cKO neurons exhibited significantly reduced AP width at 50% relative to threshold and baseline, as well as a lower AP threshold. Conversely, AP amplitude relative to both threshold and

baseline was significantly increased. Data are presented as mean ± SEM. Statistical significance was assessed using the two-tailed Mann–Whitney U test (**p < 0.01, ***p < 0.001, ****p < 0.0001). Each data point represents one cell, n = 3 mice per group.

(G) Representative images of a patch-clamped tdT-positive DA in the VTA. Upper: differential interference contrast (DIC) image showing the patched neuron. Lower: epifluorescence image showing tdTomato (RFP) expression in the same cell. Scale bar: 20 µm.

(H) Spontaneous firing of Ctrl and SJ1 cKO^{DAT} VTA DA neurons recorded in cell-attached (on-cell) configuration.

(I) Intrinsic firing of Ctrl and SJ1 cKO^{DAT} VTA DA neurons recorded in whole-cell current-clamp mode (I = 0 pA).

(J) Representative evoked firing traces in Ctrl and SJ1 cKO^{DAT} VTA DA neurons.

(K) Representative traces of the first action potential elicited in Ctrl and SJ1 cKO^{DAT} VTA DA neurons.

(L) Bar charts comparing Ctrl and SJ1cKO^{DAT} VTA DA neurons. Compared to Ctrl, SJ1 cKO^{DAT} VTA DA neurons showed a significant increase in input resistance, with no other intrinsic properties significantly altered. Data are presented as mean ± SEM. Statistical significance was assessed using the two-tailed Mann–Whitney U test (**p < 0.01, ***p < 0.001, ****p < 0.0001). Each data point represents one cell, n = 3 mice per group.

Supplementary Figure 11 Controls for lesioned models and Summary of iTHINs

(A) Representative striatum images of Ai9;DAT-Cre mice unilaterally injected with Casp3 (Cre-mediated) in the midbrain. TH-positive neurons appearing in the striatum of lesioned model (white arrows) did not show DAT-cre dependent tdT expression. Scale bar: 200 µm.

(B) Schematic illustration summarizing the proposed working model of the DA-like features of striatal iTHINs and their crosstalk with DA terminals projecting from SNc and VTA in SJ1 DA-cKO mice.

Supplementary Figure 12 Controls for SJ1 Acute KO model

(A), (B) Representative images of adult B6 mice (2 months old) (A) and aged B6 mice (12 months old) (B) unilaterally injected with AAV-TH-Cre virus show no loss of DA neurons in the midbrain or DA fibers in the striatum, validating the safety and non-toxicity of AAV TH-Cre used. Scale bar: 200 μm.

Supplementary Table 1 Electrophysiological properties of WT THINs and iTHINs

Data are represented as means ± SEM. AHP, afterhyperpolarization; AP, Action potential; Ih, hyperpolarization-activated current; LTS, low-threshold spiking; RMP, Resting membrane potential.

Supplementary Table 2 Comparison of THINs observed in WT, genetic SJ1 DA cKO and acute DA lesion mouse models

Summary of the immunostaining results and tdT expression across the striatum of control, SJ1 cKO mouse models and acute lesioned models.

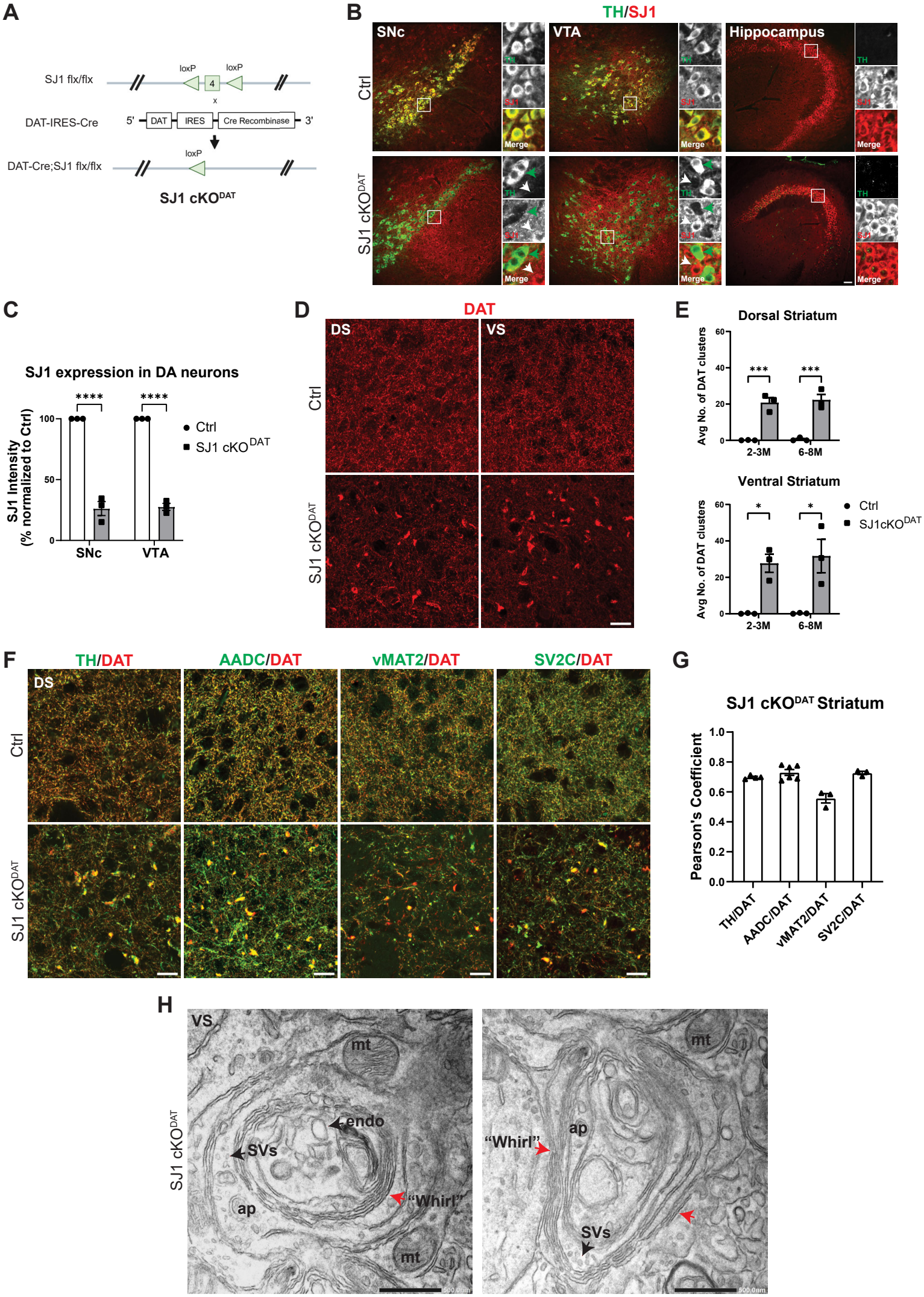
A
SJ1 flx/flx
loxP
loxP
4
x
DAT-IRES-Cre
5'
DAT
IRES
Cre Recombinase
3'
loxP
DAT-Cre;SJ1 flx/flx
SJ1 cKO^DAT
B
TH/SJ1
SNc
VTA
Hippocampus
Ctrl
SJ1 cKO^DAT
TH
SJ1
Merge
C
SJ1 expression in DA neurons
SJ1 Intensity (% normalized to Ctrl)
****
****
Ctrl
SJ1 cKO^DAT
SNc
VTA
D
DAT
DS
VS
Ctrl
SJ1 cKO^DAT
E
Dorsal Striatum
Avg No. of DAT clusters
***
***
2-3M
6-8M
Ventral Striatum
*
*
Ctrl
SJ1cKO^DAT
F
TH/DAT
AADC/DAT
vMAT2/DAT
SV2C/DAT
DS
Ctrl
SJ1 cKO^DAT
G
SJ1 cKO^DAT Striatum
Pearson's Coefficient
TH/DAT
AADC/DAT
vMAT2/DAT
SV2C/DAT
H
VS
mt
endo
SVs
ap
"Whirl"
mt
SJ1 cKO^DAT
"Whirl"
ap
SVs
mt

Figure 1

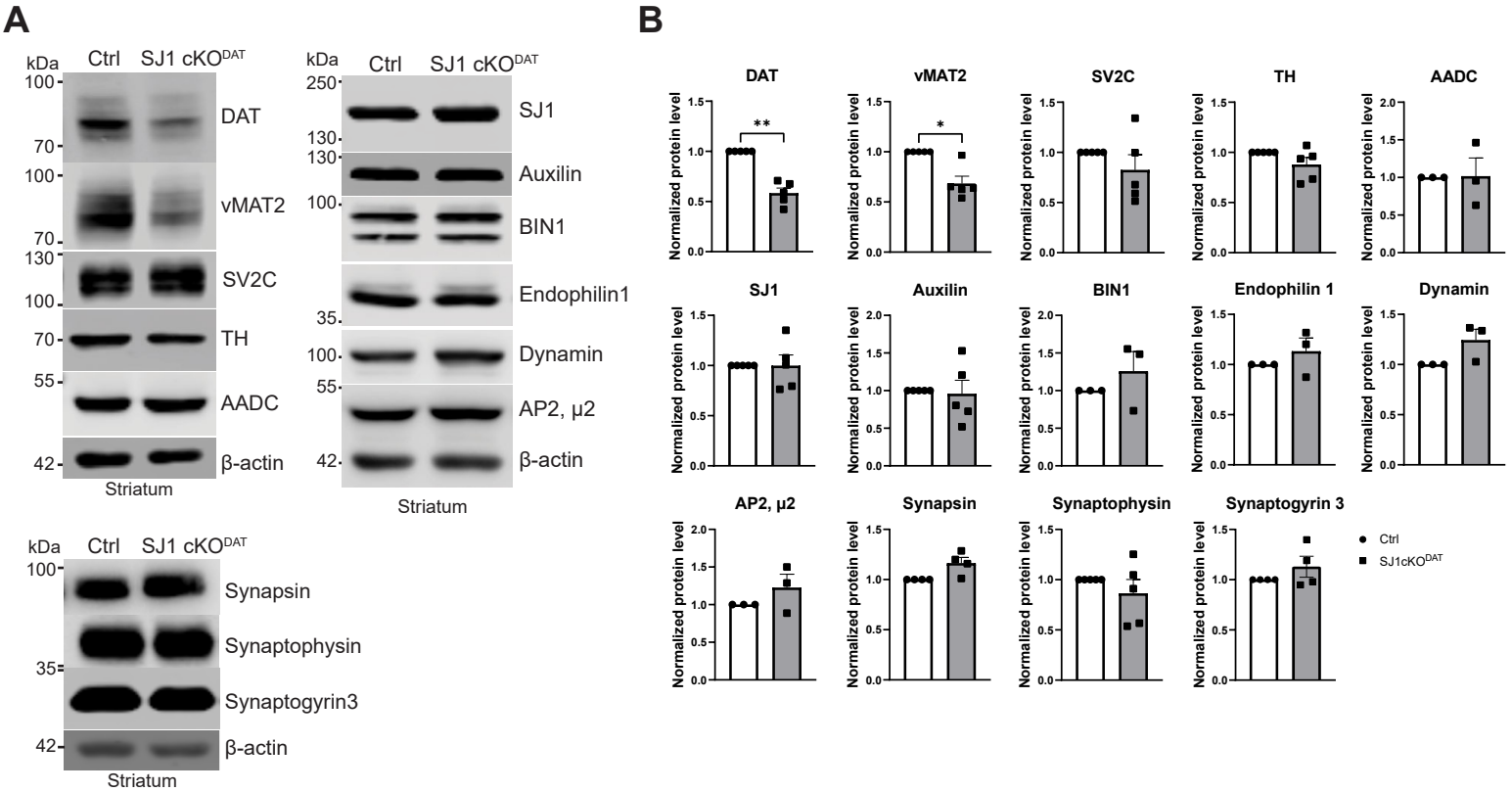
A
kDa
Ctrl
SJ1 cKO^DAT
DAT
vMAT2
SV2C
TH
AADC
β-actin
Striatum
SJ1
Auxilin
BIN1
Endophilin1
Dynamin
AP2, μ2
Synapsin
Synaptophysin
Synaptogyrin3
B
DAT
vMAT2
SV2C
TH
AADC
SJ1
Auxilin
BIN1
Endophilin 1
Dynamin
AP2, μ2
Synapsin
Synaptophysin
Synaptogyrin 3
Normalized protein level
Ctrl
SJ1cKO^DAT

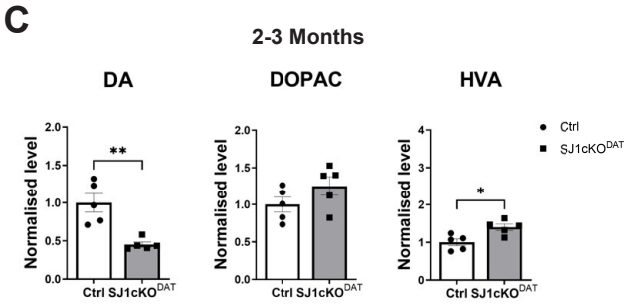
C
2-3 Months
DA
DOPAC
HVA
Normalised level
Ctrl
SJ1cKO^DAT

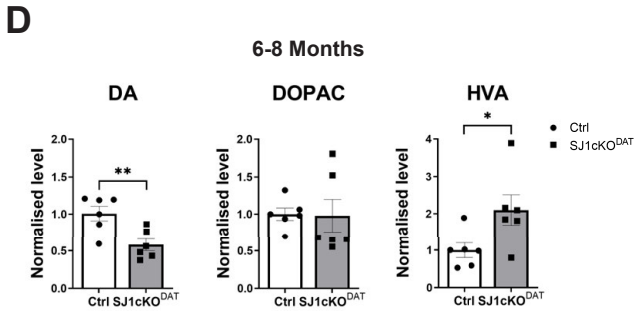
D
6-8 Months
DA
DOPAC
HVA
Normalised level
Ctrl
SJ1cKO^DAT

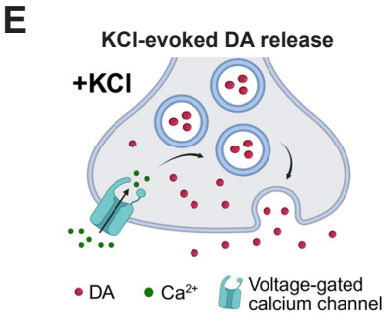
E
KCl-evoked DA release
+KCl
DA
Ca2+
Voltage-gated calcium channel

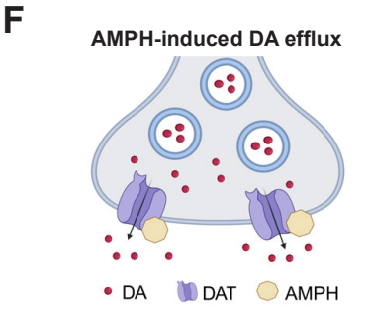
F
AMPH-induced DA efflux
DA
DAT
AMPH

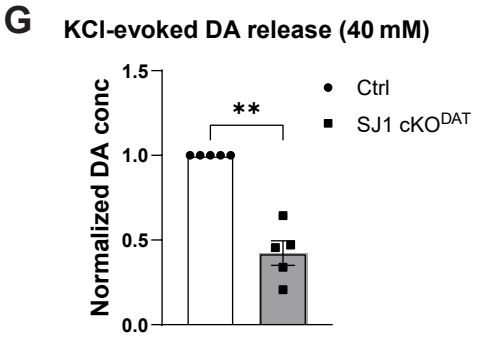
G
KCl-evoked DA release (40 mM)
Normalized DA conc
Ctrl
SJ1 cKO^DAT

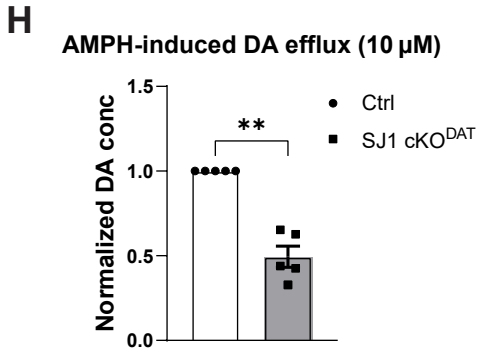
H
AMPH-induced DA efflux (10 μM)
Normalized DA conc
Ctrl
SJ1 cKO^DAT

Figure 2

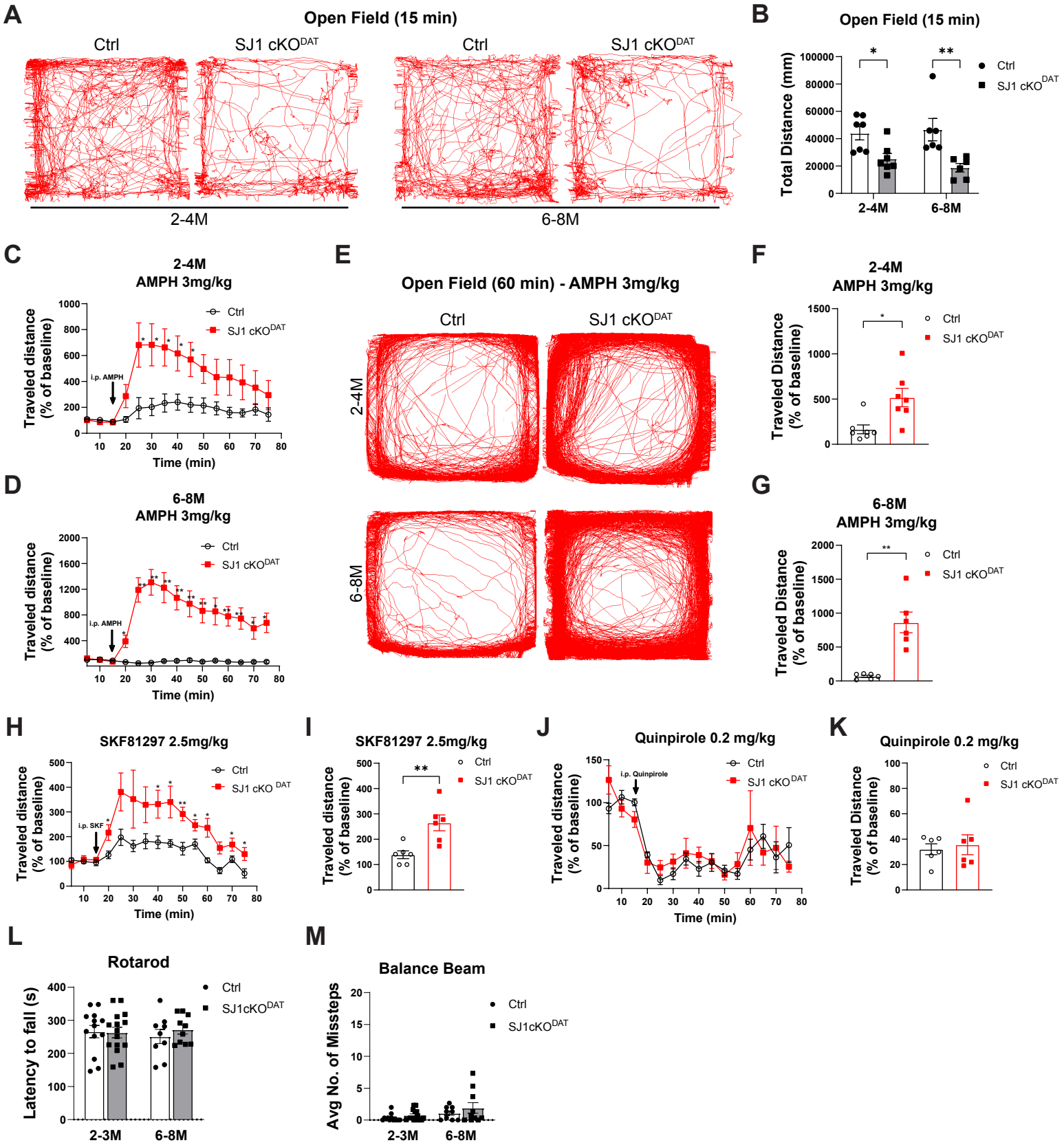
A
Open Field (15 min)
Ctrl
SJ1 cKO^DAT
Ctrl
SJ1 cKO^DAT
2-4M
6-8M
B
Open Field (15 min)
Total Distance (mm)
100000
80000
60000
40000
20000
0
*
**
Ctrl
SJ1 cKO^DAT
2-4M
6-8M
C
2-4M
AMPH 3mg/kg
Traveled distance (% of baseline)
i.p. AMPH
Ctrl
SJ1 cKO^DAT
Time (min)
D
6-8M
AMPH 3mg/kg
Traveled distance (% of baseline)
i.p. AMPH
Ctrl
SJ1 cKO^DAT
Time (min)
E
Open Field (60 min) - AMPH 3mg/kg
Ctrl
SJ1 cKO^DAT
2-4M
6-8M
F
2-4M
AMPH 3mg/kg
Traveled Distance (% of baseline)
Ctrl
SJ1 cKO^DAT
G
6-8M
AMPH 3mg/kg
Traveled Distance (% of baseline)
Ctrl
SJ1 cKO^DAT
H
SKF81297 2.5mg/kg
Traveled distance (% of baseline)
i.p. SKF
Ctrl
SJ1 cKO DAT
Time (min)
I
SKF81297 2.5mg/kg
Traveled distance (% of baseline)
Ctrl
SJ1 cKO^DAT
J
Quinpirole 0.2 mg/kg
Traveled distance (% of baseline)
i.p. Quinpirole
Ctrl
SJ1 cKO^DAT
Time (min)
K
Quinpirole 0.2 mg/kg
Traveled Distance (% of baseline)
Ctrl
SJ1 cKO^DAT
L
Rotarod
Latency to fall (s)
Ctrl
SJ1cKO^DAT
2-3M
6-8M
M
Balance Beam
Avg No. of Missteps
Ctrl
SJ1cKO^DAT
2-3M
6-8M

Figure 3

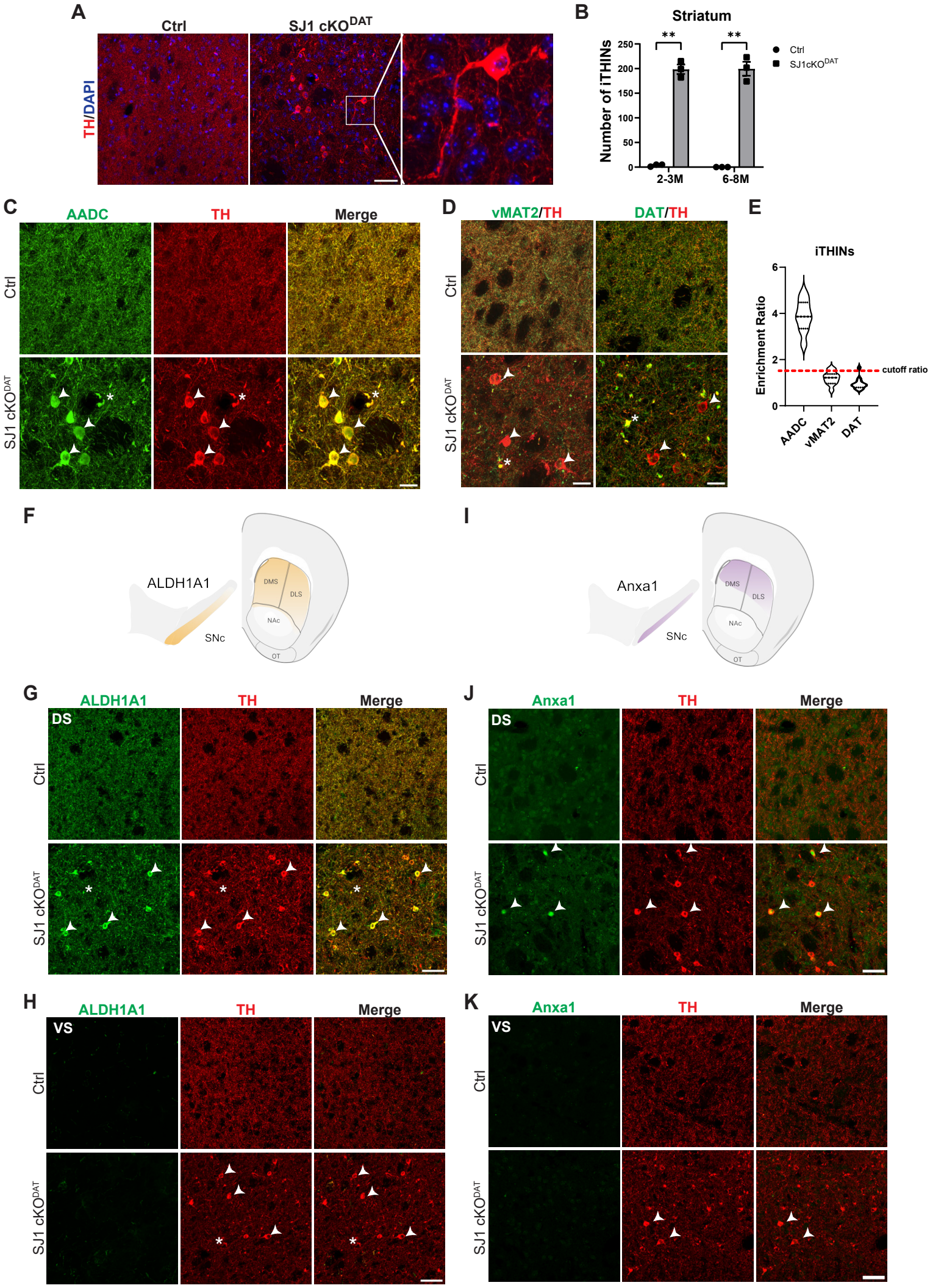
A
Ctrl
SJ1 cKO^{DAT}
TH/DAPI
B
Striatum
Number of iTHINs
250
200
150
100
50
0
**
**
2-3M
6-8M
Ctrl
SJ1cKO^{DAT}
C
AADC
TH
Merge
Ctrl
SJ1 cKO^{DAT}
D
vMAT2/TH
DAT/TH
Ctrl
SJ1 cKO^{DAT}
E
iTHINs
Enrichment Ratio
6
4
2
0
cutoff ratio
AADC
vMAT2
DAT
F
ALDH1A1
SNc
DMS
DLS
NAc
OT
I
Anxa1
SNc
DMS
DLS
NAc
OT
G
ALDH1A1
TH
Merge
DS
Ctrl
SJ1 cKO^{DAT}
J
Anxa1
TH
Merge
DS
Ctrl
SJ1 cKO^{DAT}
H
ALDH1A1
TH
Merge
VS
Ctrl
SJ1 cKO^{DAT}
K
Anxa1
TH
Merge
VS
Ctrl
SJ1 cKO^{DAT}

Figure 4

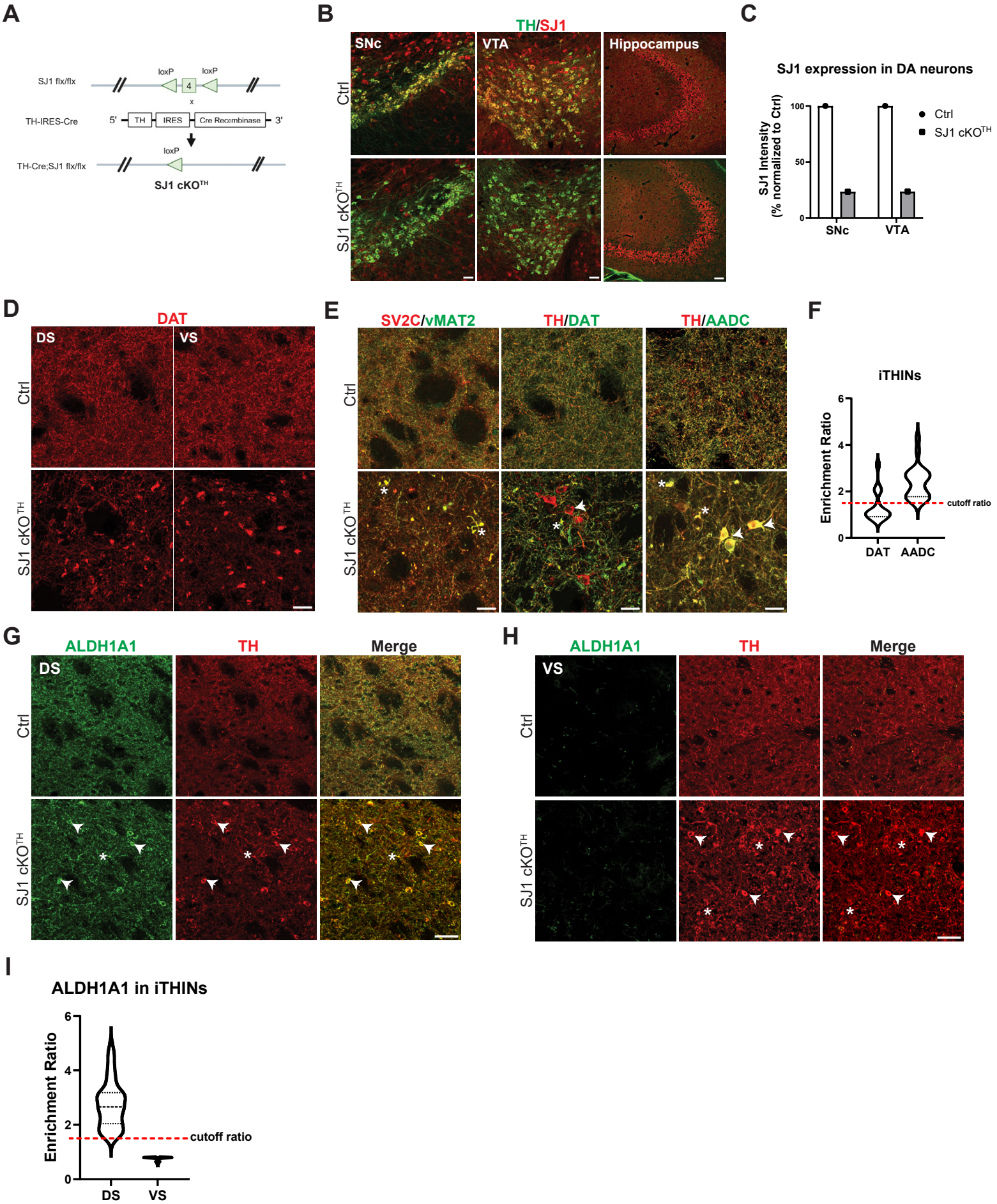
A
SJ1 flx/flx
loxP
loxP
4
x
TH-IRES-Cre
5'
TH
IRES
Cre Recombinase
3'
loxP
TH-Cre;SJ1 flx/flx
SJ1 cKO^TH
B
TH/SJ1
SNc
VTA
Hippocampus
Ctrl
SJ1 cKO^TH
C
SJ1 expression in DA neurons
SJ1 Intensity (% normalized to Ctrl)
100
50
0
SNc
VTA
Ctrl
SJ1 cKO^TH
D
DAT
DS
VS
Ctrl
SJ1 cKO^TH
E
SV2C/vMAT2
TH/DAT
TH/AADC
Ctrl
SJ1 cKO^TH
F
iTHINs
Enrichment Ratio
6
4
2
0
cutoff ratio
DAT
AADC
G
ALDH1A1
TH
Merge
DS
Ctrl
SJ1 cKO^TH
H
ALDH1A1
TH
Merge
VS
Ctrl
SJ1 cKO^TH
I
ALDH1A1 in iTHINs
Enrichment Ratio
6
4
2
0
cutoff ratio
DS
VS

Figure 5

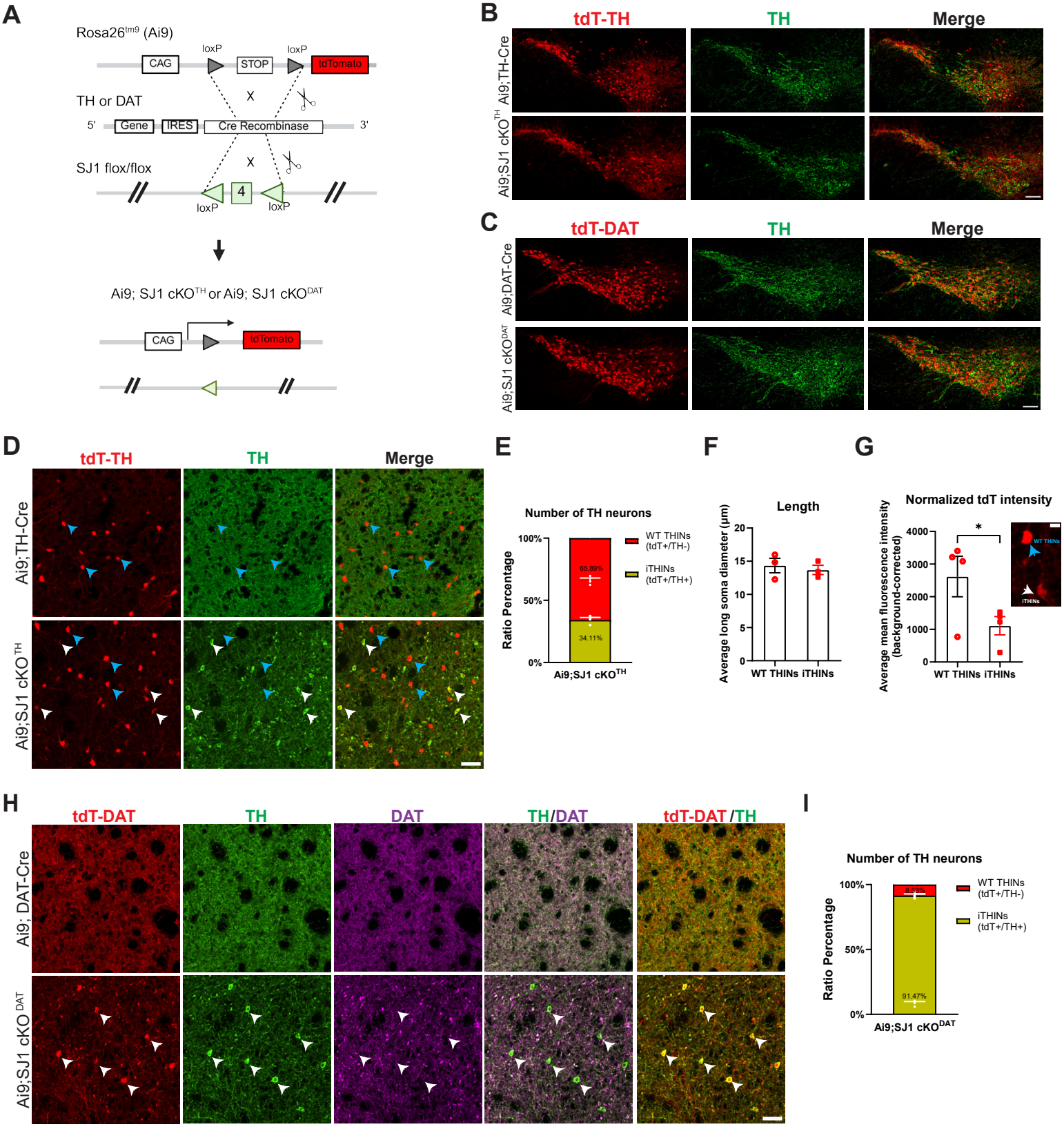
A
Rosa26trm9 (Ai9)
CAG
loxP
STOP
loxP
tdTomato
TH or DAT
5'
Gene
IRES
Cre Recombinase
3'
SJ1 flox/flox
4
loxP
loxP
Ai9; SJ1 cKOTH or Ai9; SJ1 cKODAT
CAG
tdTomato
B
tdT-TH
TH
Merge
Ai9;TH-Cre
Ai9;SJ1 cKOTH
C
tdT-DAT
TH
Merge
Ai9;DAT-Cre
Ai9;SJ1 cKODAT
D
tdT-TH
TH
Merge
Ai9;TH-Cre
Ai9;SJ1 cKOTH
E
Number of TH neurons
Ratio Percentage
100%
50%
0%
65.89%
34.11%
WT THINs (tdT+/TH-)
iTHINs (tdT+/TH+)
Ai9;SJ1 cKOTH
F
Length
Average long soma diameter (μm)
20
15
10
5
0
WT THINs
iTHINs
G
Normalized tdT intensity
Average mean fluorescence intensity (background-corrected)
4000
3000
2000
1000
0
*
WT THINs
iTHINs
H
tdT-DAT
TH
DAT
TH/DAT
tdT-DAT /TH
Ai9; DAT-Cre
Ai9;SJ1 cKODAT
I
Number of TH neurons
Ratio Percentage
100%
50%
0%
8.53%
91.47%
WT THINs (tdT+/TH-)
iTHINs (tdT+/TH+)
Ai9;SJ1 cKODAT

Figure 6

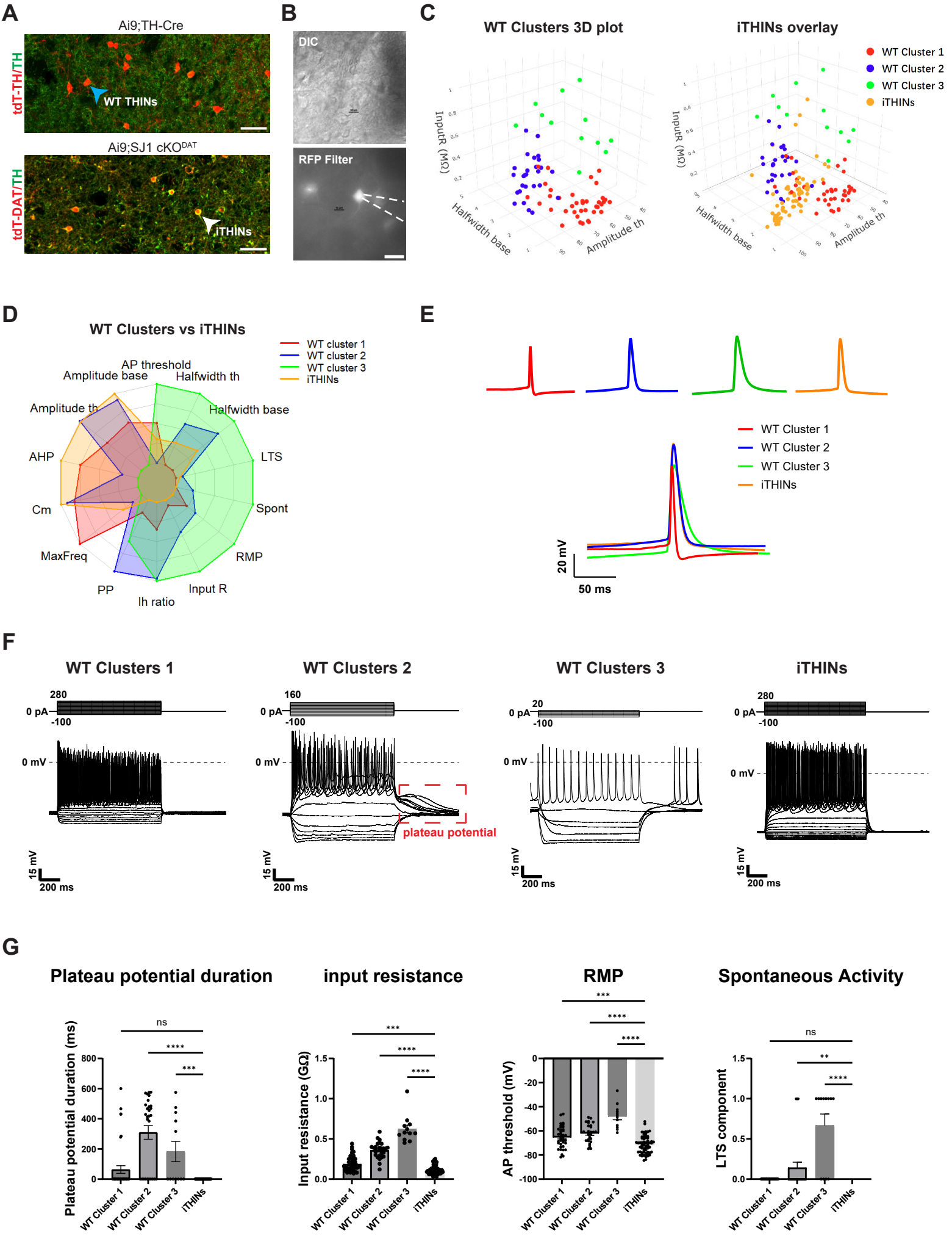
A
Ai9;TH-Cre
tdT-TH/TH
WT THINs
Ai9;SJ1 cKO^DAT
tdT-DAT/TH
iTHINs
B
DIC
RFP Filter
C
WT Clusters 3D plot
iTHINs overlay
WT Cluster 1
WT Cluster 2
WT Cluster 3
iTHINs
InputR (MΩ)
Halfwidth base
Amplitude th
D
WT Clusters vs iTHINs
WT cluster 1
WT cluster 2
WT cluster 3
iTHINs
AP threshold
Amplitude base
Halfwidth th
Amplitude th
Halfwidth base
AHP
LTS
Cm
Spont
MaxFreq
RMP
PP
Input R
Ih ratio
E
WT Cluster 1
WT Cluster 2
WT Cluster 3
iTHINs
20 mV
50 ms
F
WT Clusters 1
WT Clusters 2
WT Clusters 3
iTHINs
280
160
20
0 pA
-100
0 mV
plateau potential
15 mV
200 ms
G
Plateau potential duration
input resistance
RMP
Spontaneous Activity
Plateau potential duration (ms)
Input resistance (GΩ)
AP threshold (mV)
LTS component
ns
***
****
**
WT Cluster 1
WT Cluster 2
WT Cluster 3
iTHINs

Figure 7

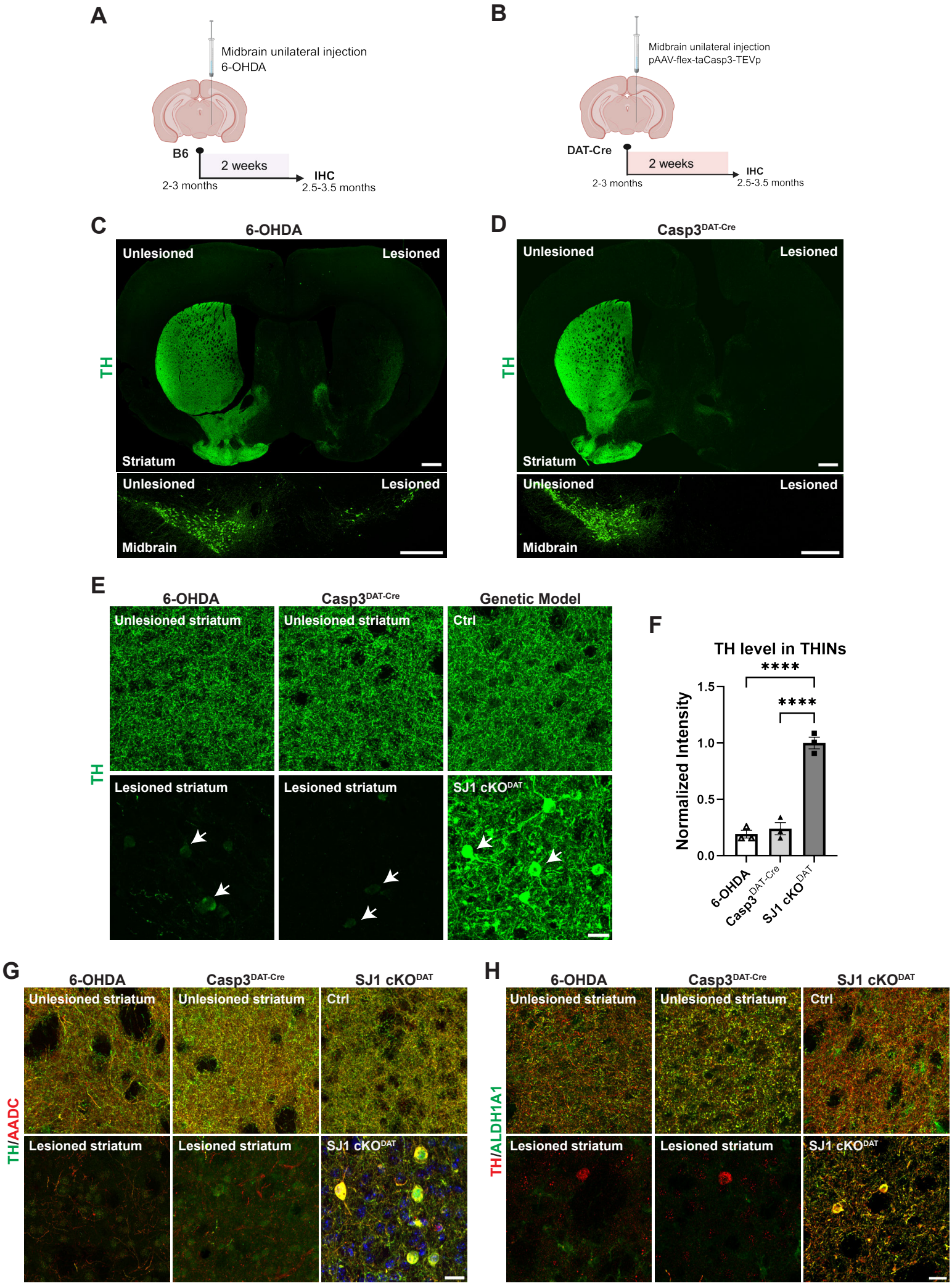
A
Midbrain unilateral injection
6-OHDA
B6
2 weeks
2-3 months
IHC
2.5-3.5 months
B
Midbrain unilateral injection
pAAV-flex-taCasp3-TEVp
DAT-Cre
2 weeks
2-3 months
IHC
2.5-3.5 months
C
6-OHDA
Unlesioned
Lesioned
TH
Striatum
Unlesioned
Lesioned
Midbrain
D
Casp3DAT-Cre
Unlesioned
Lesioned
TH
Striatum
Unlesioned
Lesioned
Midbrain
E
6-OHDA
Casp3DAT-Cre
Genetic Model
Unlesioned striatum
Unlesioned striatum
Ctrl
TH
Lesioned striatum
Lesioned striatum
SJ1 cKODAT
F
TH level in THINs
****
****
Normalized Intensity
1.5
1.0
0.5
0.0
6-OHDA
Casp3DAT-Cre
SJ1 cKODAT
G
6-OHDA
Casp3DAT-Cre
SJ1 cKODAT
Unlesioned striatum
Unlesioned striatum
Ctrl
TH/AADC
Lesioned striatum
Lesioned striatum
SJ1 cKODAT
H
6-OHDA
Casp3DAT-Cre
SJ1 cKODAT
Unlesioned striatum
Unlesioned striatum
Ctrl
TH/ALDH1A1
Lesioned striatum
Lesioned striatum
SJ1 cKODAT

Figure 8

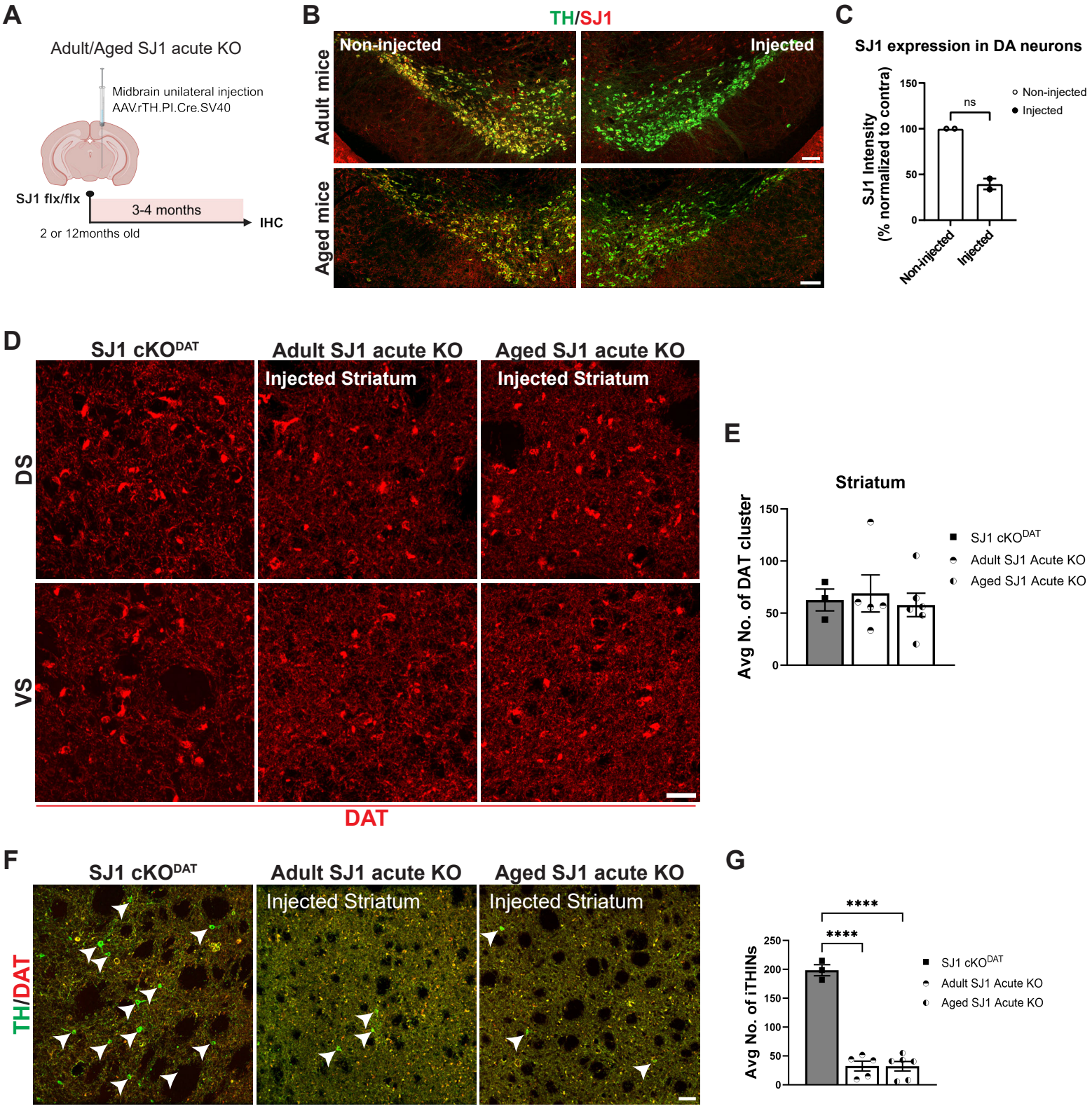
A
Adult/Aged SJ1 acute KO
Midbrain unilateral injection
AAV.rTH.PI.Cre.SV40
SJ1 flx/flx
3-4 months
IHC
2 or 12months old
B
TH/SJ1
Non-injected
Injected
Adult mice
Aged mice
C
SJ1 expression in DA neurons
SJ1 Intensity
(% normalized to contra)
150
100
50
0
ns
Non-injected
Injected
Non-injected
Injected
D
SJ1 cKODAT
Adult SJ1 acute KO
Aged SJ1 acute KO
Injected Striatum
Injected Striatum
DS
VS
DAT
E
Striatum
Avg No. of DAT cluster
150
100
50
0
SJ1 cKODAT
Adult SJ1 Acute KO
Aged SJ1 Acute KO
F
SJ1 cKODAT
Adult SJ1 acute KO
Aged SJ1 acute KO
Injected Striatum
Injected Striatum
TH/DAT
G
****
****
Avg No. of iTHINs
250
200
150
100
50
0
SJ1 cKODAT
Adult SJ1 Acute KO
Aged SJ1 Acute KO

Figure 9